Ionic Mononuclear [Fe] and Heterodinuclear [Fe,Ru] *bis*(diphenylphosphino)alkane Complexes: Synthesis, Spectroscopy, DFT Structures, Cytotoxicity, and Biomolecular Interactions

Matylda Odachowski[a], Robin Neven[a], Giuditta Perversi[a], Dario Romano[b], Cathryn A. Slabber[c], Mouna Hadiji[d], Maarten Honing[e], Yuandi Zhao[e], Orde Q. Munro[c,*], and Burgert Blom[a,*]

[a]*Maastricht Science Programme, Faculty of Science and Engineering, Maastricht University, Paul Henri Spaaklaan 1, 6229 EN Maastricht, The Netherlands*

[b]*King Abdullah University of Science and Technology, Department of Chemical Sciences, Division of Physical Sciences and Engineering, King Abdullah University of Science and Technology (KAUST), Thuwal 23955-6900, Kingdom of Saudi Arabia*

[c]*Molecular Sciences Institute, School of Chemistry, University of the Witwatersrand, PO WITS 2050, Johannesburg, South Africa*

[d]*Institut des Sciences et Ingénierie Chimiques, Ecole Polytechnique Fédérale de Lausanne (EPFL), CH1015 Lausanne, Switzerland*

[e]*Maastricht Multimodal Molecular Imaging (M4i) Institute, Division of Imaging Mass Spectrometry Maastricht University, Universiteitssingel 50, 6229ER, Maastricht, the Netherlands*

**Corresponding author e-mail addresses:*
burgert.blom@maastrichtuniversity.nl; orde.munro@wits.ac.za

Graphical Abstract

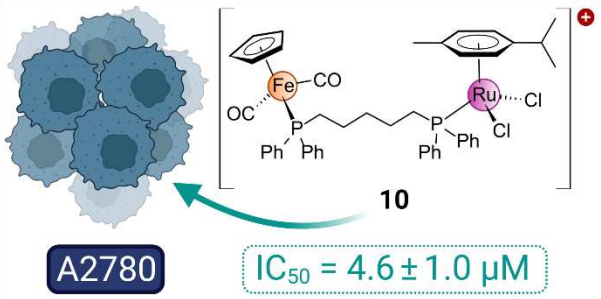

Cationic mononuclear Fe(II) and heterodinuclear [Fe^{2+}, Ru^{2+}] half-sandwich organometallic complexes interact with DNA, exhibiting significant cytotoxicity towards the human ovarian cancer cell lines A2780 and cisplatin-resistant A2780cis. The efficacy depends on the bridging *bis*(phosphane) chain length for the heterodinuclear derivatives. Protein binding (transferrin) was also detected by mass spectrometry.

Highlights

- Cationic mononuclear Fe^{2+} and heterodinuclear [Fe^{2+}, Ru^{2+}] complexes are described.
- The compounds were moderately cytotoxic *in vitro* (ovarian cancer cell line A2780).
- Cytotoxicity increases with bridging ligand chain length (dinuclear complexes).
- The DNA interaction capability increases with bridging *bis*(phosphane) chain length.
- The Ru(II) complexes have two exchangeable Cl^- ligands governing their reactivity.

Abstract

Iron(II) and Ru(II) half-sandwich compounds encompass some promising pre-clinical anticancer agents whose efficacy may be tuned by structural modification of the coordinated ligands. Here, we combine two such bioactive metal centres in cationic *bis*(diphenylphosphino)alkane-bridged heterodinuclear [Fe^{2+}, Ru^{2+}] complexes to delineate how ligand structural variations modulate compound cytotoxicity. Specifically, Fe(II) complexes of the type $[(\eta^5\text{–}C_5H_5)Fe(CO)_2(\kappa^1\text{–}PPh_2(CH_2)_nPPh_2)]\{PF_6\}$ (n = 1–5), compounds **1**–**5**, and heterodinuclear [Fe^{2+}, Ru^{2+}] complexes, $[(\eta^5\text{–}C_5H_5)Fe(CO)_2(\mu\text{–}PPh_2(CH_2)_nPPh_2))(\eta^6\text{–}p\text{–cymene})RuCl_2]\{PF_6\}$ (n = 2–5) (compounds **7**–**10**), were synthesized and characterized. The mononuclear complexes were moderately cytotoxic against two ovarian cancer cell lines (A2780 and cisplatin resistant A2780cis) with IC_{50} values ranging from 2.3 ± 0.5 μM to 9.0 ± 1.4 μM. For **7**–**10**, the cytotoxicity increased with increasing Fe···Ru distance, consistent with their DNA affinity. UV-visible spectroscopy suggested the chloride ligands in heterodinuclear **8**–**10** undergo stepwise substitution by water on the timescale of the DNA interaction experiments, probably affording the species $[RuCl(OH_2)(\eta^6\text{-}p\text{-cymene})(PRPh_2)]^{2+}$ and $[Ru(OH)(OH_2)(\eta^6\text{-}p\text{-cymene})(PRPh_2)]^{2+}$ (where $PRPh_2$ has R = $[\text{–}(CH_2)_5PPh_2\text{–}Fe(C_5H_5)(CO)_2]^+$). One interpretation of the combined DNA-interaction and kinetic data is that the mono(aqua) complex *may* interact with dsDNA through nucleobase coordination. Heterodinuclear **10** reacts with glutathione (GSH) to form stable mono- and *bis*(thiolate) adducts, **10-SG** and **10-SG$_2$**, with no evidence of metal ion reduction (k_1 = 1.07(17) × 10^{-1} min^{-1} and k_2 = 6.04(59) × 10^{-3} min^{-1} at 37 °C). This work highlights the synergistic effect of the Fe^{2+}/Ru^{2+} centres on both the cytotoxicity and biomolecular interactions of the present heterodinuclear complexes.

Keywords: ruthenium, metallodrug, cytotoxic, DNA-binding, glutathione coordination

---

Introduction

Cancer persists as one of the leading causes of death worldwide.[1] To date, platinum-based anticancer agents (e.g., cisplatin, oxaliplatin, and carboplatin) have been at the forefront of chemotherapeutics for the treatment of various cancers.[2-6] Despite the success of these complexes, their clinical application is accompanied by drawbacks such as low selectivity (leading to severe side-effects) and tumours exhibiting acquired and intrinsic drug-resistance.[7-10] These disadvantages have inspired further research on transition metal-based anticancer agents, with the overarching aim to increase their cytotoxicity and selectivity towards diseased cells alongside decreasing their undesirable side-effects.[6, 11] Notably, ruthenium and iron complexes have emerged as promising new metallodrug candidates.[11-21]

NAMI-A and KP1019 represent two significant Ru(III) complexes which entered human clinical trials,[22-26] culminating in a steady growth in the number of studies in the field since the early 1980's.[27] Much of the research in recent years has focused on half-sandwich Ru(II)-arene complexes.[28-32] Studies relating the structure of Ru(II)-arene complexes to their activity suggest that an increase in cytotoxicity

correlates with increasing hydrophobicity, a characteristic highly dependent on the nature of the arene substituents, although this does not correlate with *in vivo* activity.[33, 34] Furthermore, positively charged Ru complexes display potent anticancer activity owing to their interactions with negatively charged cell membranes – an interaction which potentially facilitates cellular uptake.[35-37] Noteworthy examples of Ru(II)-arene complexes include RAPTA-C and RM175, both of which display strong anticancer activity *in vivo*.[32, 38-41]

The success of ruthenium complexes as anticancer agents has been partially attributed to binding to the iron-delivery protein transferrin.[42] In contrast, studies suggest that Ru complexes bind rapidly to human serum albumin (HSA) – the most abundant plasma protein – rendering the percentage of these complexes available for transferrin binding insignificant, due to the higher concentration of HSA.[43-47] Nonetheless, the potential to exploit iron-binding moieties in cancer treatment need not be disregarded. Notably, iron transport in the body is predominantly facilitated by transferrin and, to a lesser extent, by other proteins such as albumin.[48] However, the successful binding of iron to transferrin is dependent on its cationic state, as well as the presence of a suitable anion.[42] Cancer cells, being metabolically demanding, present an increased number of transferrin receptors as compared to healthy cells, and thus a higher rate of iron uptake.[49-51] While also contributing to oncogenesis and the maintenance of rapid proliferation of cancer cells, iron and its relevant binding proteins can, under specific conditions, be utilised in cancer treatment. Perhaps the increased rate of iron uptake by cancer cells could provide a selective and efficient target for iron-based ionic anticancer agents.[50]

Another interesting strategy in the development of anticancer agents in recent years has been the incorporation of two distinct metal centres into a well-defined bimetallic system. Such systems present an opportunity to combine the chemical and biological features of two metals into one well-defined structure. Indeed, studies have demonstrated synergies in bimetallic systems, resulting in improved cytotoxicity compared with their mononuclear analogues.[52-56] In bimetallic systems, the bridging ligand influences the chemical and electronic dynamics between the two metals, thereby tuning the biological activity of the complexes.[57] Tertiary phosphines, which are readily available and typically stable, are often employed as bridging ligands in bimetallic systems.[58] Such ligands provide for a generally strong P–M bond (where M is a transition metal), ensuring robust linking of the two metals, thereby hindering dissociation into mononuclear entities.[59] Additionally, sterically demanding tertiary phosphines, such as *bis*(diphenylphosphino)alkanes, tend to promote monodentate bonding.[59-61] Of relevance here, a recent review highlights the fact that incorporation of two distinct metal centres in heterobimetallic compounds bridged by *bis*(diphenylphosphino)methane can enhance their cytotoxicity relative to the corresponding homobimetallic analogues.[56]

We have explored ruthenium- and iron-based complexes as potential anticancer agents. Specifically, initial investigations focused on half-sandwich Ru(II)-arene complexes bearing stannyl and germyl

ligands.[61-63] While the cytotoxicity of these complexes was suboptimal, the ionic stannate and germanate compounds display higher efficacy and selectivity *in vitro* compared with the neutral species. Concurrent research has focused on bimetallic systems (*Chart 1)*[64, 65] wherein a series of heterodinuclear [Fe^{2+}, Ru^{2+}] and homodinuclear [Ru^{2+}, Ru^{2+}] and [Fe^{2+}, Fe^{2+}] arene complexes bridged by μ-dppm were investigated. The heterobimetallic [Fe^{2+}, Ru^{2+}] systems are more selective and were more cytotoxic than both cisplatin and the dinuclear [Ru^{2+}, Ru^{2+}] systems *in vitro*.[64] Subsequently, similar heterobimetallic systems were explored, with slightly varied ligands and extended *bis*(phosphane) bridges.[65] Importantly, the novel heterobimetallic systems were highly cytotoxic compared with the homobimetallic [Fe^{2+}, Fe^{2+}] complexes. These preliminary studies have shown that neutral [Fe^{2+}, Ru^{2+}] bimetallic complexes bearing a bridging *bis*(phosphane) ligand are a promising new class of potential anticancer agents.

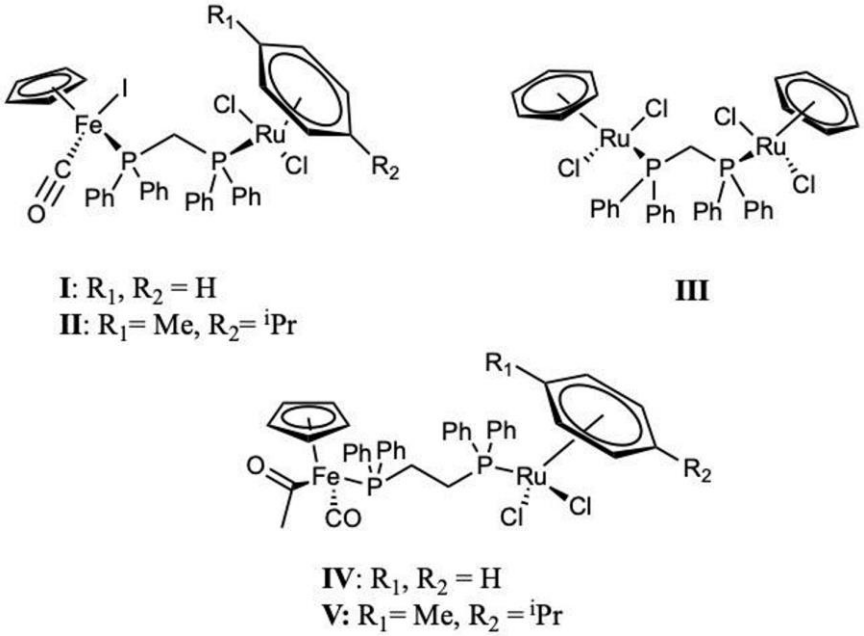

Chart 1. Concurrent research on heterobimetallic systems.[64, 65]

Here, we describe our investigations into the synthesis, characterization, and biological evaluation of ionic [Fe^{2+}] and [Fe^{2+}, Ru^{2+}] *bis*(diphenylphosphino)alkane complexes **2**–**10** (Schemes 1 and 2). The reported complexes were characterized by multinuclear NMR, FTIR, Raman, UV-visible spectroscopy and ESI-MS and tested on two cancer cell lines (alongside a non-tumorigenic cell line) principally to determine the effect of varying the alkyl chain length between the two metal centres on cytotoxicity, as well as the effect of the addition of a Ru(II) metal centre to a mononuclear Fe(II) complex. Detailed biophysical studies are also reported to help elucidate the fate of the precursor molecules *in vitro*.

Experimental

General considerations

All reactions, unless stated otherwise, were conducted under nitrogen atmosphere using Schlenk procedures. All solvents were degassed prior to use through nitrogen purging. All chemicals were obtained from commercial suppliers and used as received. Heating plates of the model RCT basic heating plate (IKA®) were used. A laboport vacuum pump (KNF lab) was used for Buchner filtrations. NMR experiments were carried out at 298 K using a Bruker Ultrashield 300 MHz/54 mm magnet system. Bruker Topspin 4.0.6 was used for NMR spectral analysis. Chemical shifts of $^{31}P\{^{1}H\}$ NMR peaks were observed relative to phosphoric acid (85%), and ^{1}H and $^{13}C\{^{1}H\}$ NMR resonance signals were measured relative to tetramethylsilane (TMS) and were reported in parts per million. FTIR analyses were carried out using MIRacle 10 Shimadzu with a single reflection ATR accessory. The Raman spectra were collected with a Renishaw inVia™ confocal Raman microscope. The crystallised samples where imaged with a Leica 50x Long Distance Objective. The Raman scattering was acquired with a 532 nm (green) diode laser with 2400 l/mm grating. Each spectrum was acquired with 20 accumulations of 1 s exposures with the laser at 0.5% power (0.1 mW) to avoid thermal decomposition. The acquired spectra were processed in the 200-2200 cm^{-1} region, the underlying fluorescence was removed with a linear baseline removal applied to all spectra before peak identification. UV-visible spectra were obtained using a UV-188 Shimadzu spectrometer and quartz suprasil precision cells (100-QS, 10 mm light path) from Hellma Analytics. The rotary evaporator consisted of three separate pieces of equipment: an IKA RV10 digital (VWR by IKA) rotational device, an IKA HB10 digital (VWR by IKA) water bath, and a KNF lab SC 920 vacuum pump. Direct injection method was utilised for EI–MS measurements performed on a GCMS–QP2010Ultra (Shimadzu). High Resolution ESI–MS measurements were obtained at Technische Universitaet Berlin where the data was acquired using an Orbitrap LTQ XL of Thermo Scientific mass spectrometer. The signals for both EI–MS and ESI–MS were thoroughly checked and compared to the theoretical isotope patterns predicted by an online software enviPat Web 2.4. The synthesis of complexes **1** ($[(\eta^5\text{–}C_5H_5)_2Fe]^+PF_6^-$), **2** ($[(\eta^5\text{–}C_5H_5)Fe(CO)_2(\kappa^1\text{–dppm})]^+PF_6^-$), and **3** ($[(\eta^5\text{–}C_5H_5)Fe(CO)_2(\kappa^1\text{–dppe})]PF_6$) was carried out according to previous literature and can be found in the supporting information.[66, 67]

Synthesis of $[(\eta^5\text{–}C_5H_5)Fe(CO)_2(\kappa^1\text{–dppp})]^+PF_6^-$ (4)

0.500 g (1.51 mmol) of **1** ($[(\eta^5\text{–}C_5H_5)_2Fe]^+PF_6^-$), 0.751 g (1.82 mmol) of dppp and 0.267 g (0.75 mmol) of cyclopentadienyl iron (II) dicarbonyl dimer were dissolved in 20 mL of degassed dichloromethane. Under a positive nitrogen pressure, the reaction mixture was stirred for 1 hour at room temperature. A dark–khaki solution was acquired and was filtered over filter paper. Subsequently, the volume of the filtrate was reduced to approximately 5 mL. Diethyl ether (35 mL) was then added dropwise, resulting in the formation of a fine yellow–green microcrystalline powder as a precipitate in a yellow solution. The supernatant was then decanted, and the precipitate was washed with diethyl ether (3 x 10 mL) and dried *in vacuo*. 0.6374 g of **4** was obtained, signifying a yield of 56%. ^{1}H NMR (300 MHz, DMSO–d_6,

298 K): δ 7.68–7.25 (20H, m, C_6H_5 dppp), 5.48 (5H, m, η^5–C_5H_5), 2.89 (2H, m, CH_2 dppp), 2.20 (2H, t, CH_2 dppp), 1.33 (1H, m, CH_2 dppp), 1.21 (1H, m, CH_2 dppp) ppm; $^{13}C\{^1H\}$ NMR (75.4 MHz, DMSO–d_6, 298K): δ 210.5 (d, $^2J_{C-P}$ = 23.9 Hz, *C*O), 210.3 (d, $^2J_{C-P}$ = 23.9 Hz, *C*O), 138.1–128.8 (m, PC_6H_5 dppp), 89.1 (s, η^5–C_5H_5), 32.7 (m, CH_2 dppp), 27.9 (m, CH_2 dppp), 21.1 (d, $^xJ_{C-P}$ = 17.2 Hz, CH_2 dppp) ppm; $^{31}P\{^1H\}$ NMR (121.4 MHz, DMSO–d_6, 298K): δ 57.6 (d, $^4J_{P-P}$ = 9 Hz, Fe–$P(C_6H_5)_2$), –18.6 (s, $FeP(C_6H_5)_2(CH_2)_2P(C_6H_5)_2$), –144.2 (sept., $^1J_{P-F}$ = 710.8 Hz, PF_6) ppm; $^{19}F\{^1H\}$ NMR (282.2 MHz, DMSO–d_6, 298K): δ –70.1 (d, $^1J_{F-P}$) = 710.7 Hz, PF_6) ppm. ESI–MS (DCM): 605.0691 (100, $C_{34}H_{31}O_3P_2Fe^+$; $[M+O]^+$; calc. 605.1098), 589.0704 (38, $C_{34}H_{31}O_2P_2Fe^+$; $[M^\bullet]^+$; calc. 589.1149), 561.0818 (25, $C_{33}H_{31}OP_2Fe^+$; $[M - CO]^+$; calc. 561.1199), 549.0804 (17, $C_{32}H_{31}OP_2Fe^+$; $[M - 2CO + O]^+$; calc. 549.1199), 533.0889 (10, $C_{32}H_{31}P_2Fe^+$; $[M - 2CO]^+$; calc. 533.1250). FTIR (cm^{-1}): υ = 3123 (w), 2367 (w), 2050 (s, *CO* stretch), 2002 (s, *CO* stretch), 1481 (w), 1435 (m), 1311 (w), 1186 (w), 1098 (m), 999 (w), 817 (s), 741 (m), 694 (s), 607 (m); UV–Vis (nm/DCM): λ = 337.5, 225, 221, 218; m.p. = 130°C. Raman (crystallised samples, 532 nm laser at 0.1 mW, 20 accumulations of 1 second) in cm^{-1}: 219, 367, 395, 510, 556, 594, 617, 686, 740, 1002, 1029, 1099,1117, 1167, 1193, 1588.

Synthesis of $[(\eta^5–C_5H_5)Fe(CO)_2(\kappa^1–dppb)]^+PF_6^-$ (5)

0.500 g (1.51 mmol) of **1**, 0.776 g (1.82 mmol) of dppb and 0.267 g (0.75 mmol) of cyclopentadienyl iron (II) dicarbonyl dimer were dissolved in 20 mL of degassed dichloromethane. Under a positive nitrogen pressure, the reaction mixture was stirred intensively for 1 hour at room temperature. A dark–khaki solution was acquired and was filtered over filter paper. Subsequently, the volume of the filtrate was reduced to 5 mL, to which diethyl ether (35 mL) was added dropwise. This resulted in the formation of a fine yellow microcrystalline powder as a precipitate with a yellow solution. The supernatant was then decanted, and the precipitate was washed with diethyl ether (3 x 10 mL) and dried *in vacuo*. 0.4386 g of **5** was obtained, resulting in a yield of 39%. ^1H NMR (300 MHz, DMSO–d_6, 298 K): δ 7.79–7.28 (20H, m, C_6H_5 dppb), 5.54 (5H, m, η^5–C_5H_5), 2.82 (2H, m, CH_2 dppb), 2.08 (2H, t, CH_2 dppb), 1.44 (4H, m, CH_2 dppb) ppm; $^{13}C\{^1H\}$ NMR (75.4 MHz, DMSO–d_6, 298K): δ 210.7 (d, $^2J_{C-P}$ = 23.9 Hz, *C*O), 138.8–129.0 (m, PC_6H_5 dppb), 89.1 (s, η^5–C_5H_5), 31.0 (d, $^xJ_{C-P}$ = 28.0 Hz, CH_2 dppb), 27.1 (d, $^2J_{C-P}$ = 16.6 Hz, CH_2 dppb), 26.3 (d, $^xJ_{C-P}$ = 11.4 Hz, CH_2 dppb), 25.5 (d, $^xJ_{C-P}$ = 16.8 Hz, CH_2 dppb) ppm; $^{31}P\{^1H\}$ NMR (121.4 MHz, DMSO–d_6, 298 K): δ 58.4 (d, $^5J_{P-P}$ = 37.2 Hz, Fe$P(C_6H_5)_2$), –17.4 (s, $P(C_6H_5)_2$), –144.2 (sept., $^1J_{P-F}$ = 711.6 Hz, PF_6) ppm; $^{19}F\{^1H\}$NMR (282.2 MHz, DMSO–d_6, 298K): δ –70.1 (d, $^1J_{F-P}$ = 711.5 Hz, PF_6) ppm; ESI–MS (DCM): 619.1731 (100, $C_{35}H_{33}O_3P_2Fe^+$; $[M+O]^+$; calc. 619.1245), 603.1700 (30, $C_{35}H_{33}O_2P_2Fe^+$; $[M^\bullet]^+$; calc. 603.1305), 575.1700 (16, $C_{34}H_{33}OP_2Fe^+$; $[M–CO]^+$; calc. 575.1351), 563.1724 (28, $C_{33}H_{33}OP_2Fe^+$; $[M – 2CO + O]^+$; calc. 563.1351), 547.1796 (4, $C_{33}H_{33}P_2Fe^+$; $[M – 2CO]^+$; calc. 547.1401), 459.2074 (80; $[dppb + CH_3OH + H^+]^+$; calc. 459.2001), 443.2044 (28; $[dppb + O + H^+]^+$; calc. 443.1688). FTIR (cm^{-1}): υ = 2969 (w), 2359 (w), 2053 (s, *CO* stretch), 1997 (s, *CO* stretch), 1559 (w), 1437 (m), 1420 (w), 1260 (m), 1095 (m), 1016 (m), 817 (s),

741 (m), 695 (s), 555 (m). UV–Vis (nm/DCM): λ = 227.50, 222.5. m.p. = 134°C. Raman (crystallised samples, 532 nm laser at 0.1 mW, 20 accumulations of 1 second) in cm^{-1}: 220, 373, 398, 517, 557, 594, 618, 699, 742, 1002, 1028, 1097, 1120, 1157, 1188, 1588.

Synthesis of [(η^5–C_5H_5)Fe(CO)$_2$(κ^1–dpppentane)]$^+PF_6^-$ (6)

0.250 g (0.775 mmol) of **1**, 0. 401g (0.91 mmol) of dpppentane and 0.134 g (0.375 mmol) of cyclopentadienyl iron (II) dicarbonyl dimer were dissolved in 20 mL of degassed dichloromethane. Under a positive nitrogen pressure, the reaction mixture was stirred intensively for 1 hour at room temperature. A dark–khaki solution was acquired and was filtered over filter paper. Subsequently, the volume of the filtrate was reduced to 5 mL and 35 mL diethyl ether were added dropwise. This resulted in the formation of a fine yellow microcrystalline powder as a precipitate with a yellow solution. The supernatant was then decanted, and the precipitate was washed with diethyl ether (3 x 10 mL) and dried *in vacuo*. 0.326 g of **6** was obtained, resulting in a yield of 55%. ^{1}H NMR (300 MHz, DMSO–d_6, 298 K): δ 7.83–7.20 (20H, m, C_6H_5 dpppentane), 5.52 (5H, m, η^5–C_5H_5), 3.28 (1H, m, CH_2 dpppentane), 2.72 (2H, m, CH_2 dpppentane), 1.95 (1H, t, CH_2 dpppentane), 1.53 (2H, m, CH_2 dpppentane), 1.26 (4H, m, CH_2 dpppentane) ppm; ^{13}C {^{1}H} NMR (75.4 MHz, DMSO–d_6, 298K): δ 210.7 (d, $^2J_{C–P}$ = 23.9 Hz, *C*O), 210.6 (d, $^2J_{C–P}$ = 23.9 Hz, *C*O), 139.1–128.8 (m, PC_6H_5 dpppentane), 89.1 (s, η^5–C_5H_5), 31.5 (m, CH_2 dpppentane), 31.0 (m, CH_2 dpppentane), 26.9 (d, $^xJ_{C–P}$ = 11.3 Hz, CH_2 dpppentane), 25.3 (d, $^xJ_{C–P}$ = 16.7 Hz, CH_2 dpppentane), 23.7 (d, $^3J_{C–P}$ = 10 Hz, CH_2 dpppentane) ppm; ^{31}P{^{1}H}NMR (121.4 MHz, DMSO–d_6, 298K): δ 58.5 (d, $^6J_{P–P}$ = 21.9 Hz, Fe*P*(C_6H_5)$_2$), –17.9 (s, *P*(C_6H_5)$_2$), –144.2 (sept., $^1J_{P–F}$ = 711.2 Hz, *P*F_6) ppm; ^{19}F {^{1}H} NMR (282.2 MHz, DMSO–d_6, 298K): δ –70.1 (d, $^1J_{F–P}$ = 711.2 Hz, P*F*$_6$) ppm; ESI–MS (DCM): 633.0881 (100, $C_{36}H_{35}O_3P_2Fe^+$; [M+O]$^+$; calc. 633.1411), 617.0894 (20, $C_{36}H_{35}O_2P_2Fe^+$; [M$^•$]$^+$; calc. 617.1462), 589.1022 (8, $C_{35}H_{35}OP_2Fe^+$; [M – CO]$^+$; calc. 589.1513), 577.1072 (18, $C_{34}H_{35}OP_2Fe^+$; [M – 2CO + O]$^+$; calc. 577.1513), 561.1129 (4, $C_{34}H_{35}P_2Fe^+$; [M – 2CO]$^+$; calc. 561.1563), 473.1555 (9; [dpppentane + CH_3OH + H$^+$]$^+$; calc. 473.2163); FTIR (cm^{-1}): υ = 3838 (w), 3750 (w), 3647 (w), 3123 (w, C–H stretch, η^5–C_5H_5), 2938 (w), 2349 (w), 2048 (s, *CO* stretch), 2000 (s, *CO* stretch), 1435 (m), 1312 (w), 1184 (w), 1098 (m), 999 (w), 817 (s), 741 (m), 694 (s), 607 (m), 579 (m), 554 (m). UV–Vis (nm/DCM): λ = 343, 227. m.p.: 136 °C.

Synthesis of [(η^5–C_5H_5)Fe(CO)$_2$(μ^1–dppe)(η^6–p–cymene)$RuCl_2$]$^+PF_6^-$ (7)

The reaction was carried out under a positive pressure of nitrogen. 0.038 g (0.062 mmol) of (*p*–cymene) ruthenium (II) chloride dimer and 0.09 g (0.127 mmol) of **3** were added to 25 mL of degassed dichloromethane. The reaction proceeded for 5 hours at reflux (50°C) under intensive stirring, acquiring a vibrant orange colour overtime. The solution was subsequently reduced in volume to approximately 10 mL and filtered over filter paper. Diethyl ether (30 mL) was added dropwise to the filtrate, resulting in the precipitation of a bright–orange microcrystalline powder. The supernatant was

then decanted, and the precipitate was washed with diethyl ether (3 x 10 mL) and dried *in vacuo*. The mass of the final product was determined to be 0.055 g (0.054 mmol), signifying a percentage yield of 42 %. ^{1}H NMR (300 MHz, DMSO–d_6, 298 K): δ 7.61 – 7.18 (20H, m, C–*H* dppe), 5.44 (5H, s, η^5–C_5H_5), 5.47 (1 H, d, $^{3}J_{H–H}$ = 6.0 Hz, *p*–cymene C–$H^{c/d}$), 5.25 (1H, d, , *p*–cymene C–$H^{a/b}$), 2.27 (1H, m, *p*–cymene C*H*$(CH_3)_2$), 1.79 (2H, s, PC*H* bridge), 1.09 (1H, t, $^{3}J_{H–H}$ = 7.0 Hz, PC*H* bridge), 0.79 (3H, d, $^{3}J_{H–H}$ = 6.9 Hz, *p*–cymene CH(C*H*$_3)_2$) ppm; ^{13}C {^{1}H} NMR (75.4 MHz, DMSO–d_6, 298 K): δ 210.3 (s, *C*O), 210.0 (s, *C*O), 133.3–129.0 (m, *C*–H dppe), 107.6 (s, *p*–cymene), 95.7 (s, *p*–cymene), 90.2 (d, $^{2}J_{C–P}$ = 4.0 Hz, *p*–cymene *C*–$H^{c/d}$), 89.1 (s, η–C_5H_5), 86.4 (d, $^{2}J_{C–P}$ = 5.3 Hz, *p*–cymene *C*–$H^{a/b}$), 30.0 (s, *p*–cymene *C*H$(CH_3)_2$), 21.6 (s, *p*–cymene CH(*C*H3)2), 17.6 (s, P*C*H bridge), 15.6 (s, P*C*H bridge) ppm; ^{31}P {^{1}H} NMR (121.4 MHz, DMSO–d_6, 298K): δ 60.9 (d, $^{3}J_{P–P}$ = 35.9 Hz, Fe–*P*$(C_6H_5)_2$), 25.2 (d, $^{3}J_{P–P}$ = 35.9 Hz, Ru– *P*$(C_6H_5)_2$, –144.2 (sept. $^{1}J_{P–F}$ = 711.2 Hz ppm; FTIR (cm^{-1}): υ = 2370 (w), 2060 (m, *CO* stretch), 2013 (m, *CO* stretch), 1481 (w), 1436 (w), 1099 (w), 841 (s), 830 (s), 572 (w), 556 (w). UV–Vis: (nm)/DMSO λmax = 345.5 nm. ESI–MS, *m/z* Calcd. For $[M–PF_6]^+$ 881.0508. Found 881.0504.

Synthesis of [(η^5–C_5H_5)Fe(CO)$_2$(μ–dppp)(η^6–p–cymene)RuCl$_2$]$^+$PF$_6^-$ (8)

Under a positive nitrogen pressure, 0.167 g (0.227mmol) of **4** was added in proportions to 0.053 g (0.087 mmol) of (η^6–*p*–cymene)ruthenium(II) chloride dimer dissolved in 25 mL of degassed dichloromethane. This reaction mixture was stirred intensively at reflux (55°C) and was monitored by *in situ* with ^{1}HNMR and ^{31}P{^{1}H}NMR spectroscopy until completion was observed after 5 h. A red–orange solution formed, which was dried under vacuo to acquire an orange–red microcrystalline powder. Subsequently, the microcrystalline powder was washed with diethyl ether (3 x 10 mL) and dried *in vacuo*. 0.1796 g was acquired, signifying a yield of 88 % was acquired. ^{1}H NMR (300 MHz, DMSO–d_6, 298 K): δ 7.75–7.17 (20H, m, C_6H_5 dppp), 5.40 (5H, m, η^5–C_5H_5), 5.37 (1H, d, $^{3}J_{H–H}$/ $^{3}J_{H–P}$ = 5.7 Hz, *p*–cymene C–*H*, $H^{c/d}$), 5.14 (1H, d, $^{3}J_{H–H}$)/ $^{3}J_{H–P}$ = 5.7 Hz, *p*–cymene C–*H*, $H^{a/b}$), 2.72 (2H, m, FePCH_2), 2.49 (1H, sept. , *p*–cymene C*H*$(CH_3)_2$), 2.21 (1H, m, CH_2 dppp), 1.70 (3H, s, *p*–cymene CH_3), 1.12 (2H, q, CH_2 dppp), 0.92 (1H, m, CH_2 dppp), 0.64 (3H, d, $^{3}J_{H–H}$ = 7.0 Hz, *p*–cymene CH(C$H_3)_2$) ppm; ^{13}C {^{1}H} NMR (75.4 MHz, DMSO–d_6, 298 K): δ 210.3 (d, $^{2}J_{C–P}$ = 23.9 Hz, *C*O), 133.7–128.4 (m, C_6H5 dppp), 106.6 (s, *p*–cymene), 94.2 (s, *p*–cymene), 90.5 (d, $^{2}J_{C–P}$ = 4.9 Hz, *p*–cymene *C*–$H^{c/d}$), 89.8 (s, η–C_5H_5), 86.02 (d, $^{2}J_{C–P}$ = 6.0 Hz, *p*–cymene *C*–$H^{a/b}$), 29.9 (s, *C*H_2 dppp), 24.1 (s, *p*–cymene *C*H$(CH_3)_2$), 22.0 (s, *C*H_2 dppp), 21.3 (s, *p*–cymene CH(*C*$H_3)_2$), 17.4 (s, *p*–cymene *C*H_3), 15.6 (s, *C*H_2 dppp) ppm; ^{31}P {^{1}H} NMR (121.4 MHz, DMSO–d_6, 298K): δ 57.5 (d, $^{4}J_{P–P}$ = 21.4 Hz, Fe–*P*$(C_6H_5)_2$), 23.9 (s, Ru–*P*$(C_6H_5)_2$), –144.2 (sept., $^{1}J_{P–F}$ = 711.5 Hz, *P*F_6) ppm; ^{19}F {^{1}H} NMR (282.2 MHz, DMSO–d_6, 298K): –70.1 (d, $^{1}J_{P–F}$ = 711.4 Hz) ppm; ESI–MS (DCM): 895.1163 (100, $C_{44}H_{45}FeRuCl_2P_2O_2^+$; [M•]+; calc. 895.0665); 801.0962 (12 ; [Ru($C_{10}H_{14}$)(Cl)$_2$(κ^1–dppp) + 2ACN + H^+]$^+$; calc. 801.1630); 699.1767 (10, $C_{37}H_{40}P_2RuCl_2O^+$; [Ru($C_{10}H_{14}$)(Cl)$_2$(κ^1–dppp) + O]$^+$; calc. 699.1280), 683.1796 (11 ;

$C_{37}H_{40}P_2RuCl^+$; [$Ru(C_{10}H_{14})(Cl)_2(\kappa^1$–dppp–Cl]$^+$; calc. 683.1337), 605.1550 (46, $C_{34}H_{31}O_3P_2Fe^+$; [(η^5–C_5H_5)$Fe(CO)_2(\kappa^1$–dppp+O]$^+$; calc. 605.1092), 589.1659 (38, $C_{34}H_{31}O_2P_2Fe^+$; [(η^5–C_5H_5)$Fe(CO)_2(\kappa^1$–dppp)]$^+$; calc. 589.1149), 561.1646 (18, $C_{33}H_{31}OP_2Fe^+$; [(η^5–C_5H_5)$Fe(CO)_2(\kappa^1$–dppp)–CO]$^+$; calc. 561.1194), 533.1695 (42, $C_{32}H_{31}P_2Fe^+$; [(η^5–C_5H_5)$Fe(CO)_2(\kappa$–dppp) – 2CO]$^+$; calc. 533.1245), 445.1910 (42; [dppp + CH_3OH + H^+]$^+$; calc. 445.1844), 183.0703 (26; [$C_{12}H_8P_2$]$^+$, calc. 183.0364); FTIR (cm^{-1}): υ = 3630 (w), , 3123 (w), 3059 (w), 2959 (w), 2928 (w), 2849 (w), 2050 (s, *CO* stretch), 2002 (s, *CO* stretch), 1483 (w), 1435 (m), 1389 (w), 1313 (w), 1261 (w), 1186 (w), 1098 (m), 1030 (w), 999 (w), 959 (w), 815 (s), 744 (m), 694 (s), 608 (m), 576 (m), 556 (m). UV–Vis (nm/DCM): λ = 227.8, 225.2, 220.4, 217.6; Decomposition temperature = 176°C. Raman (crystallised samples, 532 nm laser at 0.1 mW, 20 accumulations of 1 second) in cm^{-1}: 219, 306, 359, 408, 532, 598, 618, 696, 741, 805, 838, 1001, 1029, 1104, 1117, 1208, 1587.

Synthesis of [(η^5–C_5H_5)$Fe(CO)_2$(μ–dppb)(η^6–p–cymene)$RuCl_2$]$^+PF_6^-$ (9)

Under a positive nitrogen pressure, 0.171 g (0.228mmol) of **5** was added in portions to 0.053 g (0.087 mmol) of (η^6–*p*–cymene)ruthenium(II) chloride dimer dissolved in 25 mL of degassed dichloromethane. This reaction mixture was stirred intensively at reflux (55°C) and was monitored *in situ* with ^{1}HNMR and ^{31}P{^{1}H}NMR spectroscopy until completion was observed after 4 h and 45 min. A red–orange solution formed, which was dried *in vacuo* to acquire an orange–red microcrystalline powder. Subsequently, the microcrystalline powder was washed with diethyl ether (3 x 10 mL) and dried *in vacuo*. 0.145 g was acquired, signifying a yield of 74 % was acquired. ^{1}H NMR (300 MHz, DMSO–d_6, 298 K): δ 7.76–7.28 (20H, m, C_6H_5 dppb), 5.45 (5H, d, $^3J_{H–P}$ = 15.9 Hz, η^5–C_5H_5), 5.3 (1H, d, $^3J_{H–H}$/$^3J_{H–P}$ = 5.5 Hz, *p*–cymene C–*H*, $H^{c/d}$), 5.13 (1H, d, $^3J_{H–H}$/ $^3J_{H–P}$ = 5.6 Hz, *p*–cymene C–*H*, $H^{a/b}$), 2.74 (1H, m, CH_2 dppb), 2.56 (1H, m, *p*–cymene CH(CH_3)$_2$), 2.30 (2H, m, CH_2 dppb), 2.20 (1H, m, CH_2 dppb), 1.68 (3H, s, *p*–cymene CH_3), 1.09 (4H, m, CH_2 dppb), 0.65 (3H, d, $^3J_{H–H}$ = 7.0 Hz, *p*–cymene CH(CH_3)$_2$) ppm; ^{13}C {^{1}H} NMR (75.4 MHz, DMSO–d_6, 298 K): δ 210.7 (d, $^2J_{C–P}$ = 24.2 Hz, *C*O), 133.7–128.4 (m, C_6H_5 dppb), 106.7 (s, *p*–cymene), 93.9 (s, *p*–cymene), 90.7 (d, $^2J_{C–P}$ = 4.6 Hz, *p*–cymene *C*–$H^{c/d}$), 89.0 (s, η–C_5H_5), 85.9 (d, $^2J_{C–P}$ = 5.7 Hz, *p*–cymene *C*–$H^{a/b}$), 30.8 (s, *p*–cymene *C*H(CH_3)$_2$), 29.9 (s, *C*H_2 dppb), 25.7 (s, *C*H_2 dppb), 24.5 (s, *C*H_2 dppb), 23.7 (s, *C*H_2 dppb), 21.4 (s, *p*–cymene CH(*C*H_3)$_2$), 17.4 (s, *p*–cymene *C*H_3) ppm; ^{31}P {^{1}H} NMR (121.4 MHz, DMSO–d_6, 298K): δ 58.3 (s, Fe*P*CH_2), 22.9 (s, Ru*P*CH_2), –144.2 (sept., $^1J_{P–F}$ = 711.0 Hz, *P*F_6) ppm; ^{19}F {^{1}H} NMR (282.2 MHz, DMSO–d_6, 298K): δ –70.1 (d, $^1J_{F–P}$ = 711.1 Hz, P*F*$_6$) ppm. ESI–MS (DCM): 908.9471 (100, $C_{45}H_{47}FeRuCl_2P_2O_2^+$; [M•]$^+$; calc. 909.0821); 697.0661 (15, $C_{38}H_{42}P_2RuCl^+$; [$Ru(C_{10}H_{14})(Cl)(\kappa^1$–dppb]$^+$; calc. 697.1494); 663.1233 (100, $C_{38}H_{43}P_2Ru^+$ [$Ru(C_{10}H_{14})(\kappa^1$–dppb) + H]$^+$; calc. 663.1883), 619.0645 (7, $C_{35}H_{33}O_3P_2Fe^+$; [(η^5–C_5H_5)$Fe(CO)_2(\kappa^1$–dppb) + O]$^+$; calc. 619.1245), 603.0736 (35, $C_{35}H_{33}O_2P_2Fe$ [(η^5–C_5H_5)$Fe(CO)_2(\kappa^1$–dppb)]$^+$; calc. 603.1305), 575.0852 (10, $C_{34}H_{33}OP_2Fe^+$; [(η^5–C_5H_5)$Fe(CO)_2(\kappa^1$–dppb) – CO]$^+$; calc. 575.1351), 547.0979 (10, $C_{33}H_{33}P_2Fe^+$; [(η^5–C_5H_5)$Fe(CO)_2(\kappa$–

dppb) – 2CO]$^+$; calc. 547.1407), 459.1419 (12; [dppb + CH_3OH + H^+]$^+$; calc. 459.2001). FTIR (cm^{-1}): υ = 3128 (w), 2958 (w), 2924 (w), 2868 (w), 2856 (w), 2050 (s, *CO* stretch), 2001 (s, *CO* stretch), 1482 (w), 1434 (m), 1389 (w), 1313 (w), 1261 (w), 1184 (w), 1097 (m), 1028 (w), 999 (w), 959 (w), 876 (m), 817 (s), 744 (m), 694 (s), 609 (m). UV–Vis (nm/DCM): λ_{max} = 478.2, 373.6, 218.2. Decomposition temperature = 189 °C. Raman (crystallised samples, 532 nm laser at 0.1 mW, 20 accumulations of 1 second) in cm^{-1}: 219, 303, 357, 409, 529, 559, 591, 617, 686, 741, 801, 1001, 1028, 1102, 1195, 1588.

Synthesis of [(η^5–C_5H_5)Fe(CO)$_2$(μ–dpppentane)(η^6–p–cymene)$RuCl_2$]$^+PF_6^-$ (10)

Under a positive nitrogen pressure, 0.235 g (0.31 mmol) of **6** was added in portions to 0.053 g (0.087 mmol) of (η^6–*p*–cymene)ruthenium(II) chloride dimer dissolved in 25 mL of degassed dichloromethane. This reaction mixture was stirred intensively at reflux (55°C) and was monitored by *in situ* with ^{1}HNMR and ^{31}P{^{1}H}NMR spectroscopy until completion was observed after 11 h. A red–orange solution formed, which was dried in vacuo to acquire an orange–red microcrystalline powder. Subsequently, the microcrystalline powder was washed with diethyl ether (3 x 10 mL) and dried *in vacuo*. 0.175 g was obtained, signifying a yield of 94%. ^{1}H NMR (300 MHz, DMSO–d_6, 298 K): δ 7.94–7.35 (20H, m, C_6H_5 dpppentane), 5.52 (5H, s, η^5–C_5H_5), 5.31 (1H, , d, $^3J_{H–H}$/ $^3J_{H–P}$ = 5.1 Hz, *p*–cymene C–*H*, $H^{c/d}$), 5.21 (1H,d, $^3J_{H–H}$ = 5.2 Hz, *p*–cymene C–*H*, $H^{a/b}$), 2.68 (1H, m, CH_2 dpppentane), 2.58 (1H, m, *p*–cymene C$H(CH_3)_2$), 2.32 (2H, m, CH_2 dpppentane), 1.75 (3H, s, *p*–cymene CH_3), 1.46 (1H, m, CH_2 dpppentane), 1.24 (4H, m, CH_2 dpppentane), 1.06 (1H, m, CH_2 dpppentane), 0.92 (1H, m, CH_2 dpppentane), 0.65 (3H, d, $^3J_{H–H}$ = 7.0 Hz, *p*–cymene CH(CH_3)$_2$); ^{13}C {^{1}H} NMR (75.4 MHz, DMSO–d_6, 298 K): δ 210.7 (d, $^2J_{C–P}$ = 23.7 Hz, *C*O), 210.7 (d, $^2J_{C–P}$ = 23.6 Hz, *C*O), 133.6–128.2 (m, C_6H_5 dpppentane), 106.7 (s, *p*–cymene), 93.9 (s, *p*–cymene), 90.7 (d, $^2J_{C–P}$ = 4.6 Hz, *p*–cymene *C*–H$^{c/d}$), 89.1 (s, η–C_5H_5), 85.8 (d, $^2J_{C–P}$ = 5.5 Hz, *p*–cymene *C*–H$^{a/b}$), 31.3 (m, FeP*C*H$_2$), 30.9 (s, *p*–cymene *C*H(CH$_3$)$_2$), 30.0 (s, *C*H$_2$ dpppentane), 24.5 (s, *C*H$_2$ dpppentane), 23.6 (s, *C*H$_2$ dpppentane), 22.5 (m, *C*H$_2$ dpppentane), 21.4 (s, *p*–cymene CH(*C*H$_3$)$_2$), 17.4 (s, *p*–cymene *C*H$_3$); ^{31}P {^{1}H} NMR (121.4 MHz, DMSO–d_6, 298K): 58.4 (d, $^6J_{P–F}$ = 19.5 Hz, Fe*P*CH$_2$), 22.9 (s, Ru*P*CH$_2$), –144.2 (sept., $^1J_{P–F}$ = 711.7 Hz, *P*F$_6$); ^{19}F {^{1}H} NMR (282.2 MHz, DMSO–d_6, 298K): δ –70.1 (d, $^1J_{F–P}$ = 711.6 Hz, P*F*$_6$) ppm. ESI–MS (DCM): 922.9636 (100, $C_{46}H_{49}FeRuCl_2P_2O_2^+$; [M$^•$]+; calc. 923.0978); 828.9595 (12; [Ru($C_{10}H_{14}$)(Cl)$_2$(κ^1–dpppentane) + 2ACN + H^+]$^+$; calc. 829.1943), 617.0894 (22, $C_{36}H_{35}O_2P_2Fe^+$; [(η^5–C_5H_5)Fe(CO)$_2$(κ^1–dpppentane)]$^+$; calc. 617.1462), 561.1129 (32, $C_{34}H_{35}P_2Fe^+$; [(η^5–C_5H_5)Fe(CO)$_2$(κ–dpppentane) – 2CO]$^+$; calc. 561.1563); FTIR (cm^{-1}): υ = 3119 (w), 3061 (w), 2961 (w), 2936 (w), 2349(w), 2050 (s, *CO* stretch), 2002 (s, *CO* stretch), 1435 (m), 1261 (w), 1186 (w), 1098 (m), 1023 (w), 817 (s), 741 (m), 694 (s), 610 (m), 579 (m), 556 (m). UV–Vis (nm/DCM): λ_{max} = 379, 272, 226.4. Decomposition temperature = 197°C. Raman (crystallised samples, 532 nm laser at 0.1 mW, 20 accumulations of 1 second) in cm^{-1}: 213, 306, 365, 406, 449, 530, 617, 683, 740, 838, 1001, 1028, 1103, 1167, 1188, 1587.

Cytotoxicity studies

Human ovarian carcinoma (A2780 and A2780cis) cell lines were obtained from the European Collection of Cell Cultures. The human embryonic kidney SV40 transformed (HEK293T) cell line was generously supplied from the biological screening facility (BSF, EPFL, Switzerland). Fetal bovine serum (FBS) was purchased from Sigma, DMEM GlutaMAX media (where DMEM = Dulbecco's modified Eagle medium), RPMI 1640 GlutaMAX (where RPMI = Roswell Park Memorial Institute) and Penicillin–streptomycin were obtained from Life Technologies. The cells were cultured in RPMI 1640 GlutaMAX (A2780 and A2780cis) and DMEM GlutaMAX (HEK293T) media containing 10% heat-inactivated FBS and 1% penicillin–streptomycin at 37 °C and CO_2 (5%). To maintain cisplatin resistance, the A2780cis cell line was routinely treated with cisplatin (1 μM) in the media. The cytotoxicity was determined using the 3-(4,5-dimethyl 2-thiazolyl)-2,5-diphenyl-2H-tetrazolium bromide (MTT) assay. Stock solutions of the compounds were prepared in DMSO and diluted in medium. The solutions were sequentially diluted to give a final compound concentration range of 0–100 μM. 90 μL of the cell suspension (approximately 1.35 x 10^4 cells/well) were added to 10 μL of the diluted solutions previously added in triplicates to a flat-bottomed 96-well plates. The plates were incubated for 72 h at 37 °C. RAPTA-C and Cisplatin were used as negative (200 μM) and positive (0–100 μM) controls, respectively. 10 μL of an MTT solution prepared at 5 mg/mL in Dulbecco's phosphate buffered saline was added to the cells, and the plates were incubated for 4 hours at 37 °C. After medium aspiration, the purple formazan crystals, formed by the mitochondrial dehydrogenase activity of vital cells, were dissolved by adding 100 μL of DMSO in each well. SpectroMax M5e multimode microplate reader was used to measure the absorbance of the resulting solutions which is directly proportional to the number of surviving cells. Data requisition and procession were performed using SoftMax Pro version 6.2.2 and GraphPad prism 9 software, respectively. For normalization, untreated cells represented 100% of viability whereas cells treated with 10 μM of gambogic acid were used as a reference for 0% of viability. The reported IC_{50} values are based on the means obtained from three independent experiments, each comprising three tests per concentration level.

Electrophoresis experiments

All electrophoretic mobility shift assay (EMSA) gel electrophoresis experiments were carried out using 7 cm × 10 cm hand-cast 1.25% agarose gels dissolved in 1x TA buffer (40 mM Tris, 20 mM acetate, pH 7.6) in a Mini-Sub-Cell GT® Agarose Gel Electrophoresis System (Bio-Rad). pUC57 plasmid DNA (Invitrogen) was used as the DNA target (12.5 ng/well). Ethidium bromide (Aldrich) was used as a DNA intercalator positive control at concentrations of 0.5, 5.0, and 25 μM. Cisplatin (Aldrich) was used as a DNA nucleobase covalent binder positive control at concentrations of 0.5, 5.0, and 25 μM. DMSO or DMF at 10% V/V was used as the negative control since this concentration of cosolvent was present

in all wells containing added compounds. Organometallic compounds were assayed at five doses of 5, 10, 25, 50, and 100 μM. Reactions (10.0 μL final working volume, 25 ng pUC57 DNA, 1x TA buffer, 10% DMSO or DMF) were performed in LoBind Eppendorf microcentrifuge tubes (500 μL) and incubated for 30 min at 37 °C prior to the addition of 2 μL of 6x DNA loading dye (Sigma product no. G 7654; 0.25%(w/v) bromophenol blue, 0.25%(w/v) xylene cyanole FF, 40%(w/v) sucrose in water). The dye-containing samples were then loaded (6.0 μL per well) and the gel electrophoresed at 75 V for 90 minutes at room temperature (23 °C). All gels were stained with an ethidium bromide solution (0.5 mg/L in Type 1 ultrapure water) for 20 minutes prior to rinsing (de-staining) in Type 1 ultrapure water for 20 minutes and visualizing using a G:Box Chemi XRQ gel doc system (Syngene) with mid-wave UV transillumination and a UV filter (GeneSys 1.4.6.0). Note that all compound samples were freshly prepared for each EMSA experiment by dissolving the solid (ca. 10 mg) in 1.0 mL of DMSO or DMF to give a suitable stock solution. Sonication of the solids in the solvent was *not* required to dissolve them. Where gels are repeated, the same stock solutions of the samples were used (stored at 4 °C until needed). Image analysis (densitometry) was performed with GeneTools 4.3.10 to integrate DNA band profiles for all lanes and to obtain R_f values for specific bands.

Observations on Compound Stability. None of the compounds were stable over longer periods in the usual 1x TAE (Tris-Acetate-EDTA) buffer used for electrophoresis (40 mM Tris-acetate and 1 mM EDTA, pH 8.3), even when fresh stocks were used. This was likely a result of demetallation of the organometallic complexes by EDTA or their reaction with EDTA to form new species in solution. For this reason, the gel-casting and running buffers used here were EDTA-free (i.e., simple TA buffer). The compounds were also observed to be unstable in both DMF and DMSO over a period of 7 days. Initial EMSA gels using compound stocks prepared in DMF in TA buffer and gels recorded 7 days later (identical experimental protocol) using the same stock solutions were significantly different, suggesting ligand exchange and conversion to new metal-containing species over time, e.g., complexes solvated at the Ru(II) ion (where a solvent ligand such as DMF or DMSO slowly replaces one or both coordinated chloride ligands). After dilution into the aqueous reaction buffer for the DNA interaction assay by gel electrophoresis, further solvolysis (aquation) of the complexes is possible, giving new species (e.g., Ru(II) aqua/hydroxo derivatives—see Scheme 3) that can react differently with the DNA in the EMSA experiments. The same phenomenon was encountered when using stock solutions prepared in DMSO. The compounds were, however, reasonably stable over a period of ~24 hours as gels recorded to assess the stability of the compounds in TAE and TA buffer from stock solutions made up in DMF did not show significant changes in the DNA composition for gels run 24 hours apart.

Solution stability and reactions with glutathione

Electronic spectra were recorded at 37 °C in quartz cells with a Perkin-Elmer Lambda 365 UV-visible-NIR spectrometer (200–1100 nm) fitted with a Peltier-thermostatted cell array. UV Express (Version 4.1.2, Perkin-Elmer) was used to record and process spectra. Stock solutions were freshly made due to the instability of the compounds in solution.

Compound stability experiments were performed in a TRIS-acetate buffer (40 mM TRIS base, 20 mM sodium acetate, pH 7.6) containing 10% (v/v) DMSO to solubilize the complexes, with a final compound concentration of 1.00×10^{-4} M. (TRIS = 2-amino-2-(hydroxymethyl)propane-1,3-diol.) Sample temperatures were maintained at 37 °C, with spectra recorded at 5-minute intervals for the first 15 minutes, then at 15-minute intervals until the total time of the reaction reached 4 hours. Spectra were also recorded in pure DMSO under the same conditions. For compound **7**, the absorbance at 343 nm was plotted as a function of time, t, (in minutes) and the rate constants k_I and k_{II} obtained from fitting the biphasic data to the Gompertz, $y = a \cdot \exp(-\exp(-k_I \cdot (t - t_c)))$, and Weibull, $y = a - (a-b) \cdot \exp(-(k_{II} \cdot t)^d)$, rate equations, respectively, for the two well-separated phases (i.e., distinct steps) of the reaction. In these equations, a, b, t_c, d, k_I, and k_{II} are adjustable empirical parameters obtained by nonlinear least-squares fitting of the experimental data.

L-Glutathione (GSH) stability experiments were performed in a 90% (V/V) DMSO/H_2O solution, with samples held at 37 °C for 12 hours with spectra recorded at 5-minute intervals for the first hour, followed by scans every 30 minutes. Samples were prepared at a compound concentration of 1.00×10^{-4} M, with three GSH concentrations employed: 1.00×10^{-4} M (1x), 1.50×10^{-4} M (1.5x) and 2.00×10^{-4} M (2x).

Density Functional Theory (DFT) calculations

Density functional theory (DFT) calculations were performed to model the complexes **7**-**10** using the Guassian09/GaussView 5.0.9 software package.[68a] The level of theory used for all the calculations was B3LYP[68b-e] with the basis set DEF2-TZVP used for all the atoms. Geometry optimisations were accomplished without any constraints. All optimised geometries had no imaginary frequencies. Energies and IR spectra were calculated using the optimised structures and the latter compared with experimental IR data showing a good agreement. In the case of simulations aimed at delineating experimental electronic spectra and reaction products with glutathione, Gaussian16 was employed, and the calculations were effected at the CAM-B3LYP[69]/SDD[70] level of theory in DMSO or water (default solvent polarization continuum model, PCM[71]) using the GD3BJ[72] empirical dispersion correction method as well as no dispersion correction for comparison. Electronic spectra were computed using time-dependent DFT (TD-DFT[73]). The CAM-B3LYP functional takes long-range electron correlation into account and improves the accuracy of electronic spectra calculations.

Mass spectrometry (MS) method for transferrin binding assay

Compound **9** was dissolved in dichloromethane to give a 10 mM stock solution. Transferrin was freshly prepared in water at a concentration of 1 mg/mL (stock solution). For MS measurements, compound **9** was diluted in 75% acetonitrile: 25% water (0.1% V/V acetic acid) to give a final concentration of 10 µM. Transferrin was diluted in water (0.1% V/V formic acid) to give a final concentration of 0.2 mg/mL. Thereafter, 10 µM compound and 0.2 mg/mL transferrin were incubated in a water bath at 37 °C for 1 hour. All samples were measured with a Synapt G2 (Waters) instrument employing an electrospray ionization (ESI) source using the following conditions: capillary voltage = 2.0 kV, sampling cone voltage = 100 V, cone gas flow rate = 30 L/hour, and source temperature = 150 °C. Data were acquired in positive ESI mode, with a scan rate of 1 s per scan. Acquired data were analysed with MassLynx 4.1 and UniDec 4.1.1 software.

Results and Discussion

Synthesis and spectroscopic characterisation of the ionic mononuclear κ¹-phosphane iron complexes 2–6

The synthetic route of compounds **2**–**6** was adapted from literature.[67] Of these compounds, **2** and **3** have been previously reported.[74] The one-pot reactions involve the oxidative cleavage of the cyclopentadienyl iron dicarbonyl dimer by ferrocenium hexafluorophosphate (**1**), prepared according to literature.[66] Subsequently, *bis*(diphenylphosphino)methane (dppm), *bis*(diphenylphosphino)ethane (dppe), *bis*(diphenylphosphino)propane (dppp), *bis*(diphenylphosphino)butane (dppb), and *bis*(diphenylphosphino)pentane (dpppentane) coordinated to the Fe centre to produce **2**, **3**, **4**, **5**, and **6**, respectively, in moderate to high yields as yellow, green or olive solids (Scheme 1*).*

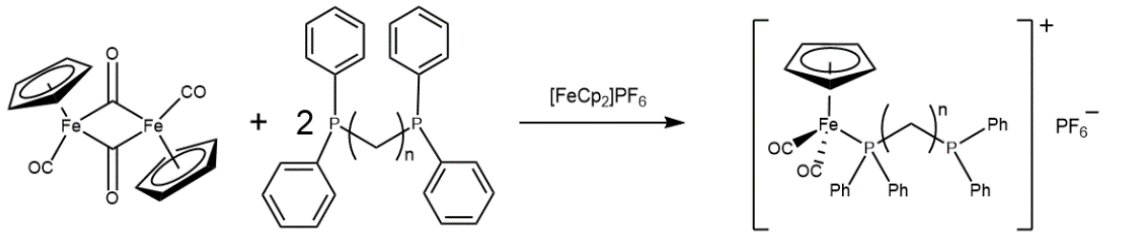

n = 1 (compound **2**) yield 80%; turquiouse solid
2 (compound **3**) yield 15%; light green solid
3 (compound **4**) yield 56%; yellow-green solid
4 (compound **5**) yield 39%; yellow solid
5 (compound **6**) yield 55%; yellow solid

Scheme 1. Synthesis of the mononuclear k^1- iron complexes **2**–**6**.

Mononuclear complexes **2**–**6** were fully characterised by multinuclear NMR, FTIR, Raman, UV-visible spectroscopy and ESI-MS. FTIR analysis confirmed two CO stretching vibrations for all complexes

corresponding to the CO symmetric and asymmetric stretching vibrations (see Table 1). ^{1}H NMR spectroscopy was used to confirm the presence of the Cp ligand as well as the aromatic H atoms of the *bis*(diphenylphosphino)alkane ligands, which in all cases clearly showed the CH_2 of the bridging phosphane in the methylene envelope region and the C_5H_5 as a singlet resonance at δ 5.46–5.54. The ^{31}P{^{1}H} NMR spectra revealed the successful complexation of the *bis*(diphenylphosphino)alkane ligands to the Fe centres in κ^1- fashion. The presence of two P atoms of dppm, dppe, dppp, dppb, and dpppentane was confirmed through two sets of doublets in each spectrum, corresponding to the Fe-bound P atom (low field shifted) and the pendant uncoordinated P atom of each ligand. Additionally, a septet at δ −144.2 was observed in each spectrum, confirming the presence of the PF_6^- counterion. High resolution ESI-mass spectrometry confirmed the identity of the complexes, all exhibiting similar fragmentation patterns. Typically, the spectra contained the M^+ peak as well as the $[M+O]^+$ (due to oxidation of the pendant P atom of the κ^1-phosphine) followed by a series of fragments corresponding to decarbonylation from these two species: $[M-CO]^+$, $[M-2CO+O]^+$ and $[M-2CO]^+$, all corresponding to the theoretically predicted isotope patterns.

Table 1. FTIR and $^{31}P\{^{1}H\}$ NMR spectroscopic data for complexes **2**–**10.**

	FTIR (cm^{-1})		$^{31}P\{^{1}H\}$ NMR			
	CO (stretching)		Fe**P**Ph$_2$PPh$_2$	FePPh$_2$(CH$_2$)$_n$**P**Ph$_2$	Fe**P**Ph$_2$(CH$_2$)$_n$ PPh$_2$Ru	FePPh$_2$(CH$_2$)$_n$ **P**Ph$_2$Ru
2	2065	2013	δ 60.4 ppm (d, $^{2}J_{P-P}$ = 88.8 Hz)	δ –24.5 ppm (d, $^{2}J_{P-P}$ = 88.8 Hz)	-	-
3	2058	2010	δ 62.4 ppm (d, $^{2}J_{P-P}$ = 41.5 Hz)	δ –14.5 ppm (d, $^{2}J_{P-P}$ = 41.5 Hz)	-	-
4	2050	2002	δ 57.6 ppm (d, $^{4}J_{P-P}$ = 9 Hz)	δ –18.6 ppm (s)	-	-
5	2053	1997	δ 58.4 ppm (d, $^{5}J_{P-P}$ = 37.2 Hz)	δ –17.4 ppm (s)	-	-
6	2048	2000	δ 58.5 ppm (d, $^{6}J_{P-P}$ = 21.9 Hz)	δ –17.9 ppm (s)	-	-
7	2060	2013	-	-	δ 60.9 ppm (d, $^{3}J_{P-P}$ = 35.9 Hz)	δ 25.2 ppm (d, $^{3}J_{P-P}$ = 35.9 Hz)
8	2050	2002	-	-	δ 57.5 ppm (d, $^{4}J_{P-P}$ = 21.4 Hz)	δ 23.9 ppm (s)
9	2050	2001	-	-	δ 58.3 ppm (s)	δ 22.9 ppm (s)
10	2050	2002	-	-	δ 58.4 ppm (d, $^{6}J_{P-F}$ = 19.5 Hz)	δ 22.9 ppm (s)

Synthesis and spectroscopic characterisation of the ionic heterodinuclear μ-diphosphane complexes 7–10

The synthesis of the heterobimetallic complexes **7**–**10** was carried out as shown in Scheme 2. The mononuclear κ^1-diphosphane iron complexes **3**–**6** were reacted with (*p*-cymene)ruthenium(II) chloride dimer resulting in the cleavage of the Ru dimer and the coordination of the pendant P atom to the Ru centre to produce **7**–**10**, respectively. Interestingly, an excess of starting materials **2**–**6** was required to bring the reactions to completion, as indicated by monitoring the reactions by ^{1}H and ^{31}P *in situ* NMR spectroscopy. All complexes were isolated in moderate to high yields, typically as orange to red powders and are thermally robust and stable in air. Interestingly, the reaction of **2** with (*p*-cymene)ruthenium(II) chloride dimer afforded the desired product i.e., [(CO$_2$(η^5-C$_5$H$_5$)Fe(μ-dppm)RuCl$_2$(η^6-*p*-cymene)]PF$_6$ on the basis of heteronuclear NMR spectroscopic data, but over time this product underwent decomposition and could not be isolated in pure form. This is likely due to the close proximity of the two metal centres with a relatively short tether.

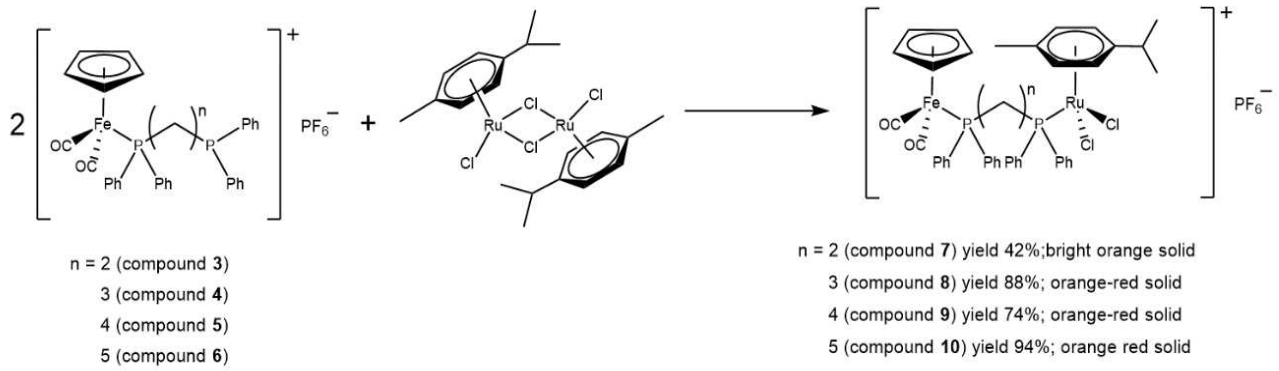

Scheme 2. Synthesis of the mononuclear heterodinuclear [Fe^{2+},Ru^{2+}] complexes **7**–**10**.

The FTIR spectra of **7**–**10** confirmed the presence of two CO ligands on the Fe centre through the occurrence of two separate stretching vibrations, corresponding to symmetric and asymmetric stretching vibrations of the individual CO ligands (Table 1). The ^{1}H NMR spectra displayed peaks in the aromatic region corresponding to 20 H atoms of the *bis*(diphenylphosphino)alkane ligands, along with a singlet resonance signal corresponding to the protons of the Cp ligand. The presence of the *p*-cymene moiety was additionally confirmed through peaks corresponding to the 4 aromatic H atoms, as well as peaks corresponding to all 7 H atoms of the $CH(CH_3)_2$ substituent of *p*-cymene (the two methyl groups and the methine proton). The $^{31}P\{^{1}H\}$ NMR analysis revealed the presence of two sets of signals corresponding to both the Fe-bound and Ru-bound P atoms of the *bis*(diphenylphosphino)alkane bridges. The downfield shift of the doublets corresponding to the pendant P atom in the $^{31}P\{^{1}H\}$ NMR spectra of complexes **2**–**6** confirms the complexation of the pendant P atom to the Ru centre in complexes **7**–**10**. Like complexes **2**–**6**, the presence of the PF_6^- counterion is confirmed through the presence of a septet at δ −144.2 in the spectra of complexes **7**–**10**. Furthermore, fragmentation patterns of complexes **7**–**10** were observed through ESI-MS and confirmed by isotope modelling. Calculated values for $[M]^+$ matched well with the observed values for each complex. Additionally, further fragmentation of **8** to $[Ru(C_{10}H_{14})(Cl)_2(\kappa^1\text{-dppp}) + 2ACN + H^+]^+$, $[Ru(C_{10}H_{14})(Cl)_2(\kappa^1\text{-dppp}) + O]^+$, $[Ru(C_{10}H_{14})(Cl)_2(\kappa^1\text{-dppp})–Cl]^+$, complex **9** to into $[Ru(C_{10}H_{14})(Cl)_2(\kappa^1\text{-dppb})–Cl]^+$ and $[Ru(C_{10}H_{14})(Cl)_2(\kappa^1\text{-dppb})–2Cl+H^+]^+$, and complex **10** to $[Ru(C_{10}H_{14})(Cl)_2(\kappa^1\text{-dpppentane})+2ACN+H^+]^+$ was observed and confirmed through calculated values. Attempts to obtain crystals suitable for single crystal X-ray diffraction investigations of all the compounds reported here were unsuccessful, even after exhaustive attempts for >1 year. Presumably this is due to the increased conformational flexibility of the complexes due to the long alkane chain between the P atoms of the coordination P atoms.

The stability of complexes **7**, **8**, **9** and **10** in DMSO-d_6 over 48 h was studied using ^{1}H and $^{31}P\{^{1}H\}$ NMR spectroscopy (Figures S56–S63). From the apparently invariant nature of the proton NMR spectra

obtained at t = 0 h, t = 24 h, and t = 48 h, it is possible that complexes **7**–**10** are quite stable in DMSO-d_6, or that any solvation of the metal ions wherein DMSO substitutes the chloride ligands coordinated to the Ru(II) centre occurs on a *shorter* timescale than required to make up the solutions and commence data acquisition after auto shimming and tuning the sample within the NMR spectrometer. From the ^{31}P NMR spectra of the complexes, however, the appearance of several lower-intensity signals for the P nucleus coordinated to the Ru(II) ion (20–25 ppm region), particularly in the case of **10**, suggests that DMSO may indeed substitute the chloride ligands affording several solution species. This question of solvent exchange is examined further in relation to the interaction of the compounds with key biomolecules such as DNA and glutathione (*vide infra*). Importantly, the NMR spectra clearly indicate that no major compound degradation (complete ligand dissociation, reduction of the metal ions, etc.) occurs in DMSO over a prolonged period. Given that DMSO is the vehicle used in cytotoxicity studies, compound stability is an important parameter as typically stock solutions of the compounds are prepared in this solvent, diluted with culture medium, and then used to dose the cell lines of interest.

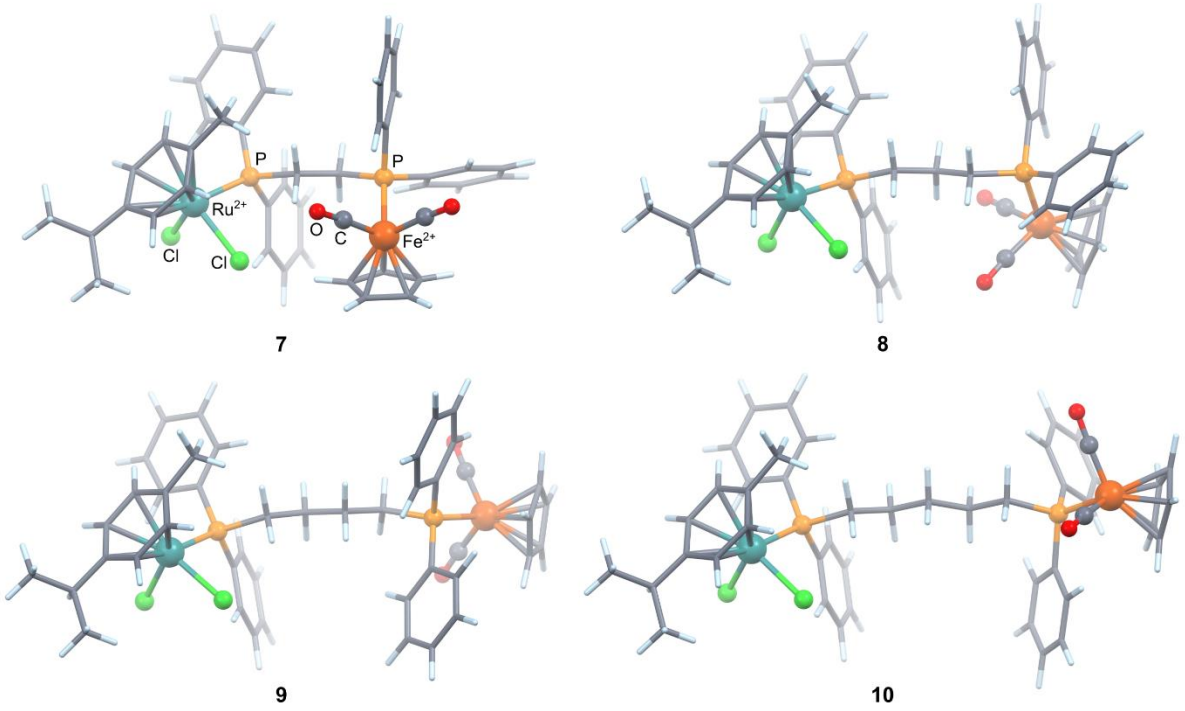

Figure 1. Geometry optimised structures (gas phase) for cationic dinuclear complexes **7–10** calculated using DFT simulations at the B3LYP/DEF2-TZVP level of theory. The charge for each cation is +1. Element colours: orange = iron, teal = ruthenium, red = oxygen, grey = carbon, yellow-orange = phosphorus, green = chlorine, blue-white = hydrogen. The IR spectra were calculated and compared to the experimentally obtained spectra showing good to excellent agreement.

Density Functional Theory DFT calculations

Complexes **7**–**10** were modelled using density functional theory (DFT) to obtain the optimised structures and the location of the frontier orbitals and their respective energies. The resulting optimised structures of complexes **7**–**10** are shown in Figure 1. From the frequency calculations for the complexes, it was possible to compute the theoretical IR spectra in the gas phase for comparison with spectra recorded for the synthesized complexes. The DFT-calculated IR spectra for **7**–**10** were very similar as expected from their small aliphatic structural differences (Figures S68B and S69). Importantly, the DFT-calculated IR spectra were in good agreement with the experimental IR spectra for the examined complexes (e.g., Figures S68A). The congruency between the theoretical and experimental IR spectra for the complexes confirms the accuracy of the structural models determined using DFT methods.

The DFT-calculated intramolecular Fe---Ru distances are summarised in Table 2 for complexes **7**–**10**. Consistent with the generally extended structures of the aliphatic chains in the low energy conformations of the complexes (Figure 1), the internuclear separation of the metal ions increases monotonically with increasing chain length, as gauged by the number of carbon atoms in the *bis*(phosphane) bridging ligand. The length of the aliphatic spacer in these compounds had a rather profound effect on the cytotoxicity, solution physical chemistry, and biomolecule affinity of the cations (*vide infra*).

Table 2. Calculated coordination group bond distances and through-space metal---metal distances for complexes **7–10**. Metal–ring centroid distances are included for the π-bonded ligands. The DFT model was checked by comparing the calculated IR spectra vs the experimentally obtained IR spectra in all cases showing excellent agreement (see SI).

Complex, C spacer	**Fe---Ru (Å)**	**Mean Ru–Cl (Å)**	**Ru–P (Å)**	**Ru–Cy (Å)**	**Fe–P (Å)**	**Mean Fe–CO (Å)**	**Fe–Cp (Å)**
7, 2C	6.457	2.47(4)	2.393	1.792	2.291	1.79(3)	1.752
8, 3C	8.283	2.46(2)	2.393	1.794	2.293	1.794(1)	1.755
9, 4C	10.721	2.46(2)	2.400	1.789	2.296	1.789(1)	1.753
10, 5C	11.788	2.46(2)	2.393	1.794	2.294	1.789(2)	1.753

The frontier orbitals (highest occupied molecular orbital (HOMO) and lowest unoccupied molecular orbital (LUMO)) were computed and evaluated for complexes **7**–**10**. As examples, Figure 2 shows the HOMO and LUMO for complexes **7** and **10**, which have the shortest and longest tether spacing, respectively. (The analogous data for **8** and **9** are available in the SI.) For all complexes, the LUMO is mainly delocalised on the iron and somewhat on the carbonyl groups, the phosphane bound to iron and on the arene moeity. The HOMO is delocalised on the ruthenium, chlorines, phosphine bound to ruthenium and, to a lesser extent, on the aromatic structure of the *p*-cymene ring.

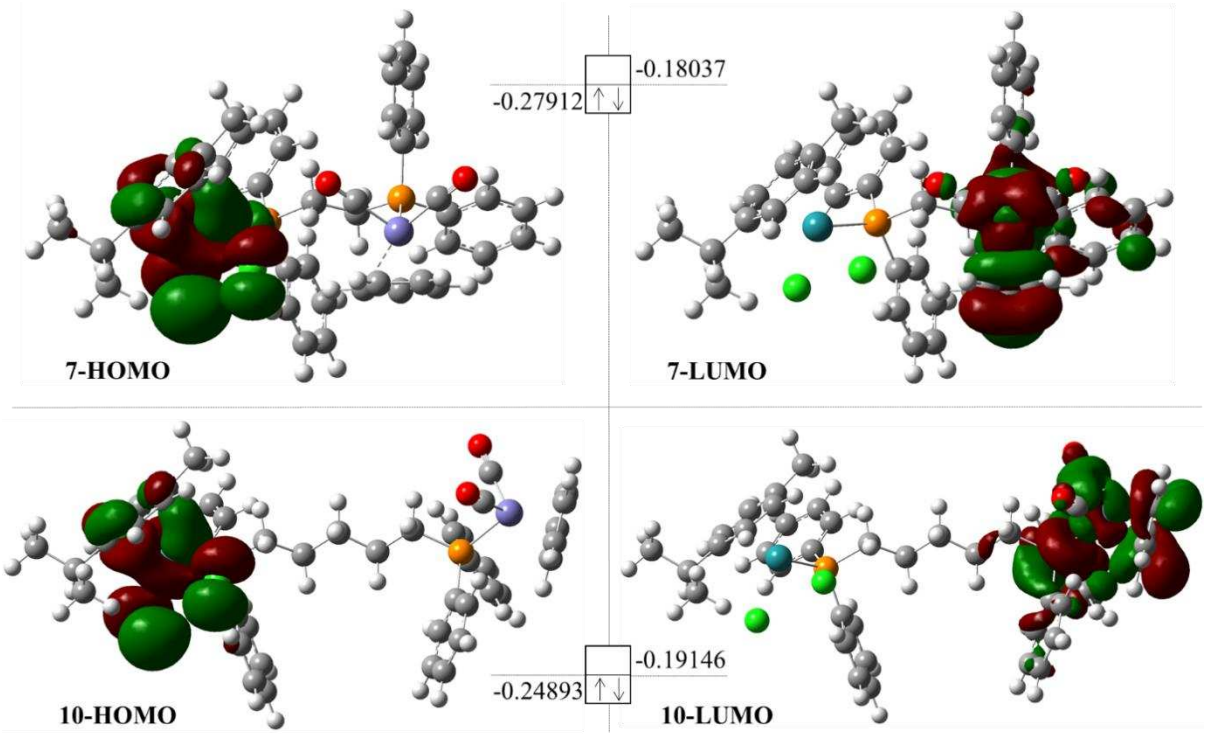

Figure 2. Homo (left) and LUMO (right) for complexes **7** (top) and **10** (bottom). HOMO and LUMO energy values are expressed in Hartree. Colours of atoms: cyan = ruthenium, orange = phosphorus, grey = carbon, white = hydrogen, green = chlorine, purple = iron.

The LUMO-HOMO energy gap decreases as a function of number of carbon atoms in the diphosphane ligand (see SI) and, interestingly, appears to govern the cytotoxicity of the complexes — this in addition to the clear dependence of the cytotoxicity on the intramolecular Fe----Ru distance or bridging diphosphane ligand chain length for these derivatives (see below and SI).

Cytotoxicity of compounds 2–10

The cytotoxicity of **2**–**10** was evaluated on the human ovarian cancer cell line A2780, the cisplatin resistant A2780cis variant and on healthy human embryonic kidney HEK293T cell line. The resulting IC_{50} values are compared to the positive control cisplatin and negative control Rapta-C in Table 3.

Table 3. IC_{50} values (μM) of **2**–**10** on A2780, A2780cis and HEK293T cells. Standard deviations are shown after the mean value.

	A2780	**A2780cis**	**Hek293T**
Compound	IC_{50}	IC_{50}	IC_{50}
2	2.3 ± 0.5	2.5 ± 0.4	2.3 ± 0.1
3	7.3 ± 5.1	6.3 ± 2.1	8.1 ± 7.2
4	5.0 ± 1.5	7.4 ± 2.2	6.9 ± 4.2
5	9.0 ± 1.4	13.5 ± 1.0	8.6 ± 1.5
6	8.3 ± 3.0	11.1 ± 2.7	8.5 ± 2.2
7	6.7 ± 1.2	12.1 ± 3.0	7.1 ± 2.6
8	7.9 ± 1.3	9.2 ± 2.2	5.4 ± 0.4
9	6.9 ± 0.9	8.2 ± 0.5	4.6 ± 0.7
10	4.6 ± 1.0	5.8 ± 0.8	3.3 ± 1.3
cisplatin	1.3 ± 0.8	8.8 ± 3.2	3.4 ± 1.3
RAPTA-C	>200	>200	>200

All complexes display a moderate cytotoxic activity toward both ovarian cancer cell lines, complex **2** being the most cytotoxic in the series with IC_{50} values of 2.3 ± 0.5 and 2.5 ± 0.4 μM on the A2780 and A2780cis cell lines, respectively. In comparison to cisplatin, complex **2** shows a superior cytotoxicity on the A2780cis cell line and a similar potency on the A2780 cell line, making it an interesting alternative compound for the cisplatin resistant cell line. This striking result is highlighted graphically in Figure S70a (Supporting Information). Several other complexes from both the mononuclear class and the dinuclear class have a similar toxicity compared to cisplatin on the A2780cis cell-line (**3**, **4**, **9** and **10**), with IC_{50} values for the two ovarian cancer cell lines being similar for each compound. The cytotoxicity of the heterodinculear complexes appears to increase in parallel with the length of the linker, most notably with complex **10** when compared to complex **7**, with IC_{50} = 5.8 ± 0.8 and 12.1 ± 3.0 μM respectively on the A2780cis cell line (cf. **Figure *3***). This might be due to the increasing hydrophobic character of the compounds as the linker increases in length, or possibly due to higher conformational flexibility between the linked metal ions (Fe^{2+}, Ru^{2+}), a notion supported by the DNA-interaction studies (*vide infra*, Figure 5).

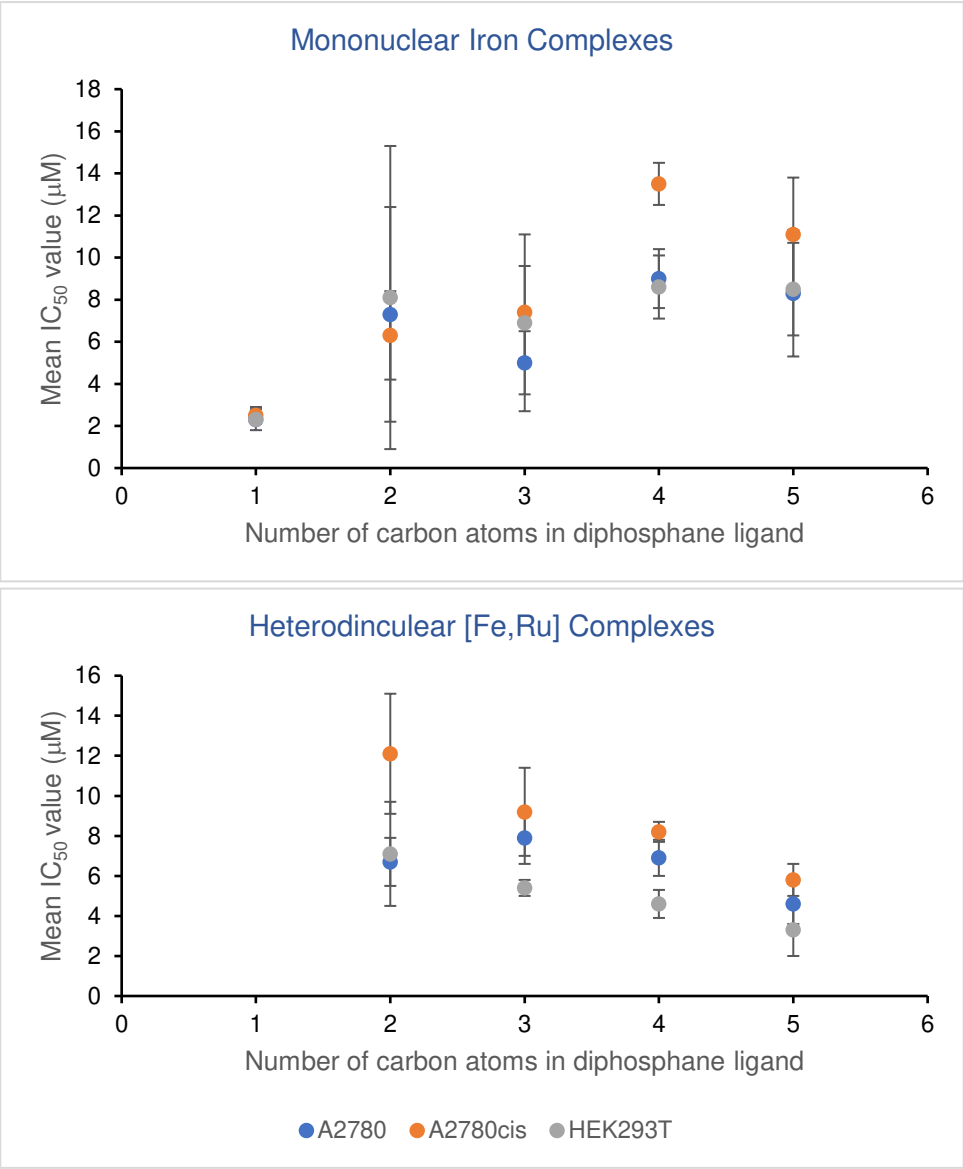

Figure 3. IC_{50} (μM) vs number of carbon atoms in diphosphane ligand for mononuclear iron complexes (top) and heterodinuclear complexes (bottom) on all three cell-lines. Standard error of the mean (SEM) included per data point.

A further noteworthy correlation is the relationship between the calculated LUMO-HOMO energy gap and cytotoxicity for the dincuclear complexes (Figure 4). A larger LUMO-HOMO gap correlates with a decrease in cytotoxicity and concomitant increase in IC_{50} values across all three cell-lines. Generally, small LUMO-HOMO energy gaps in complexes of transition metal ions, including Ru(II) arene and cyclopentadienyl derivatives,[75] imply a softer metal centre which favours a more reactive metal complex[76] capable of faster ligand substitution reactions.[77] For the present compounds, complexes with smaller LUMO-HOMO gaps are anticipated to undergo ligand exchange to produce the key cytotoxic species more readily after cellular uptake. Indeed, a more reactive Ru(II) centre with aqua ligands is more capable of binding to DNA, or reacting with oxygen to activate it to form reactive oxygen species, thereby effecting the necessary cellular level damage that may initiate apoptosis.[78]

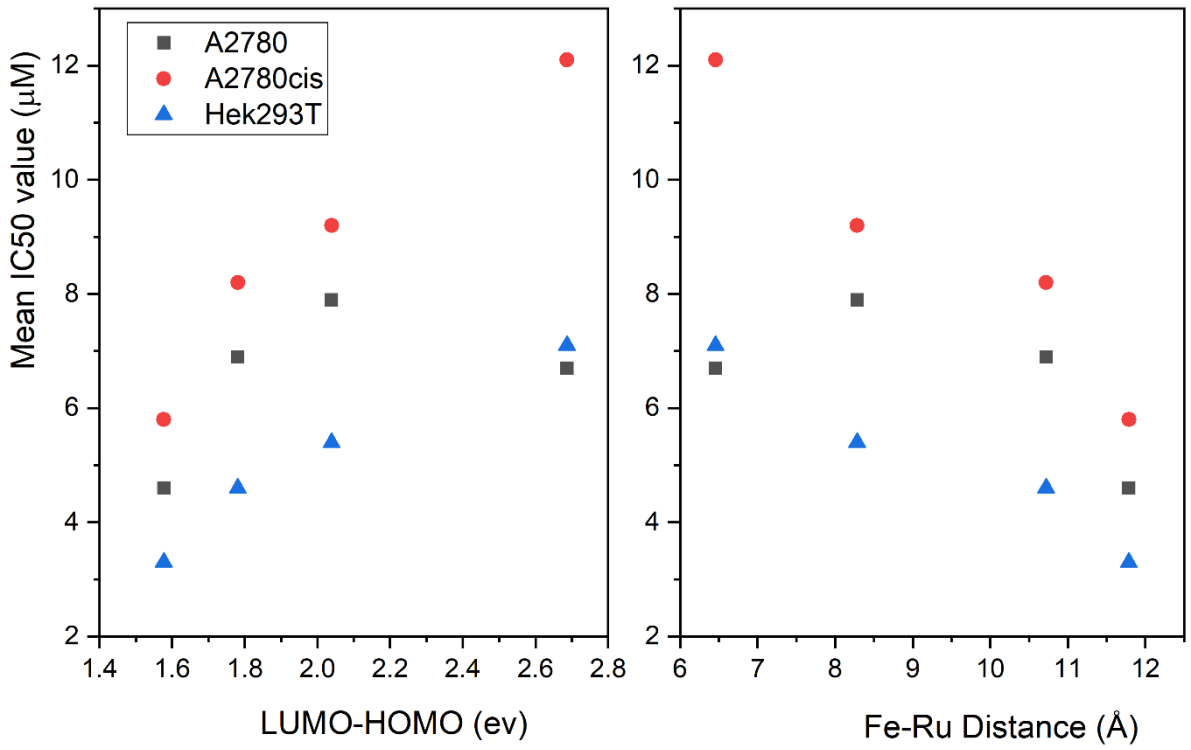

Figure 4. Plot of mean IC_{50} (μM) vs LUMO-HOMO gap in complexes **7**–**10** (Left). Plot of IC_{50} (μM) vs computed Fe-Ru distance (right).

Interaction with DNA

Since several cytotoxic metal complexes, including clinically deployed metallodrugs such as cisplatin, are known to induce apoptosis by binding to genomic dsDNA (and dsDNA *in vitro*), thereby disrupting gene transcription and DNA replication,[78] we elected to elucidate the affinity of **2**–**10** for dsDNA *in vitro* to gain an initial understanding of whether dsDNA might be a potential target for these compounds.

Broad Compound Screen. The compounds were screened at four doses (from 100 nM to 50 μM) against a fixed concentration of pUC57 plasmid DNA under identical conditions to determine whether they interact with DNA using an electrophoretic mobility shift assay (EMSA, Figure 5). Compounds **3** and **4** did not induce an electrophoretic mobility (EM) shift with increasing compound dose, while **5** and **8**–**10** gave distinct EM shifts at doses of 50 μM. Bands containing supercoiled (SC) and nicked open-circular (NOC) DNA showed larger EM shifts relative to those comprising linear DNA for **5** and **8**–**10**. Since the migration of DNA in an agarose gel is retarded when adduct formation involves intercalation or covalent base binding, which elongate or kink[79] the double helix, respectively, the results indicate that **5** and **8**–**10** form adducts with the macromolecular target via one (or possibly both) of these mechanisms. Importantly, none of the compounds caused the DNA to precipitate directly in

the wells over the concentration ranges tested (see Figure S71, Supporting Information), which can occur with poly(ionic) DNA-binding agents.[80, 81]

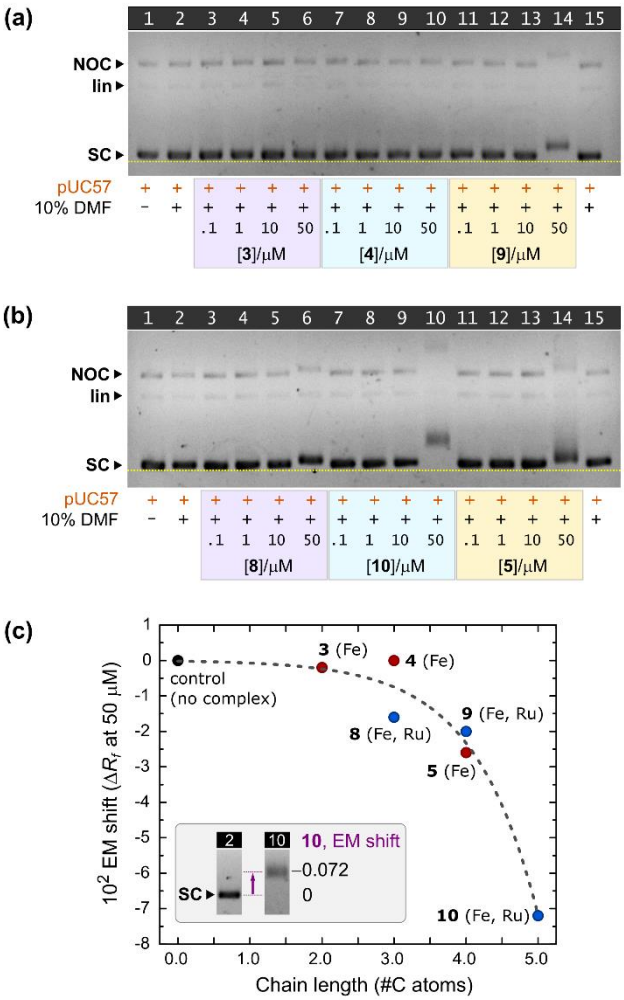

Figure 5. EMSA screen of DNA binding for compounds **3**, **4**, **5**, and **8**–**10**. Dose-dependent changes in the mobility of pUC57 plasmid DNA (2710 base pairs) containing three forms (supercoiled, SC, linear, lin, and nicked open-circular, NOC) are shown for **3**, **4**, and **9** in (a); the equivalent gel for **8**–**10** is shown in (b). Controls (plasmid with no added metal complex) were run in lanes 1, 2, and 15. Significant electrophoretic mobility (EM) shifts are observed at concentrations of 50 μM for **5** and **8**–**10**. (c) Plot of the EM shift recorded at compound concentrations of 50 μM as a function of the chain length of the *bis*(phosphane) ligand present in each organometallic complex. The inset shows how the EM shift was measured from the integrated peak profiles of SC pUC57 in the absence (lane 2) and presence (lane 10) of compound **10**.

To quantify the magnitude of the interaction with DNA at a compound dose of 50 μM for the complexes, we plotted the EM shift as a function of the number of carbon atoms making up the linker chain in the *bis*(phosphane) ligand (Figure 5c). The mobility of the SC and NOC DNA bands decreases exponentially with increasing chain length with the effect commencing at a chain length ≥ 3 carbon atoms (SC, supercoiled; NOC, nicked-open circular). There are insufficient data to establish definitively whether the dinuclear (Fe, Ru) complexes generally impact DNA more significantly than the

mononuclear Fe complexes. While the similarity in the EM shift data for **5** and **9** might suggest that Ru(II) is not particularly important for DNA binding for these two complexes (each containing a 4-carbon P–C_n–P ligand), Ru(II) clearly enhances the interaction with DNA for **8** when compared with **4** (3-carbon P–C_n–P ligand). Considering the available literature on di(chloro)ruthenium(II) arene complexes, this result likely reflects replacement of the two chloride ligands by up to 2 water ligands[82] (or H_2O/OH)[83, 84] on Ru(II) in **8**, which is a well-known reaction in mononuclear RAPTA-type complexes (RAPTA = $RuCl_2(\eta^6$-*p*-cymene)(pta), where pta = 1,3,5-triaza-7-phosphatricyclo[3.3.1.1]-decane) and a key requirement for DNA binding.[85, 86] Full or partial aquation of **8** would increase the overall charge of the complex (from +1 to +2), thereby enhancing the electrostatic contribution to DNA binding. Aquation of **8** (and the other Ru^{2+}-containing complexes) would also produce, initially, the aqua or aqua/hydroxo complexes which conceivably react with DNA like cisplatin and cross-link guanine bases via guanine N7 coordination.[87, 88] This interpretation of the data is consistent with a thorough study[89] of the aquation, DNA-, and guanine-binding reactions of a Ru(II) arene complex bearing a single exchangeable chloride ligand and an inert bidentate ligand, namely [RuCl(η^6-*p*-cymene)(DAT)]BF_4, where DAT = 6-(pyridin-2-yl)-1,3,5-triazine-2,4-diamine. Other RAPTA-type complexes, $RuCl_2(\eta^6$-*p*-cymene)(pta) and $OsCl_2(\eta^6$-*p*-cymene)(pta), also covalently bind DNA bases[90] and oligonucleotides and markedly distort the conformation of the macromolecule.[91] Importantly, kinked and cross-linked (both intra- and intermolecular) plasmid DNA species would be expected to have a less compact shape and commensurately larger hydrodynamic radius, leading to reduced mobility through the agarose gel matrix.[92] Reduced DNA mobility would also result from covalent binding (coordination) of cationic Ru(II) complexes and thus partial charge neutralization of the anionic poly(phosphate) DNA backbone.

The behaviour of **8**–**10** with plasmid DNA, especially the large negative mobility shift seen for the supercoiled form of pUC57, mirrors the observations reported by Allardyce *et al.*[93] for the reaction of [Ru(η^6-*p*-cymene)Cl_2(pta)] with pBR322 DNA as a function of pH. However, **8**–**10** also reduce the mobility of the NOC form of pUC57, unlike the mononuclear Ru(II) complex. This quite possibly reflects the more elaborate structures of the binuclear complexes studied here and a possible role played by the $[Fe(Cp)(CO)_2]^+$ moiety or bridging *bis*(phosphane) ligand in governing the manner in which the compounds interact with NOC pUC57 DNA. Compound **10** with a 5-carbon P–C_n–P ligand linking the two metal centres exhibits the largest EM shift for this series of compounds when measured at a dose of 50 μM. Since none of the compounds interact significantly with pUC57 DNA at a dose of 10 μM, the binding constants are all likely to be in a similar range with dissociation constants (K_d values) significantly larger than 10 μM. (As discussed later, the reactivity of the metal complexes studied here unfortunately precludes quantitative measurement of their DNA affinity constants.) The substantial negative EM shift for **10** evidently reflects the degree to which the compound alters the DNA structure and its hydrodynamic radius rather than the extent of the equilibrium (i.e., binding constant) at 50 μM.

One possible explanation is that **10** primarily binds to DNA via covalent interaction of one or more nucleobases with the Ru(II) ion, along with additional, secondary interactions involving the longer linker chain for **10**. In principle, this could accommodate more complex binding modes such as partial intercalation or threading intercalation involving the *bis*(phosphane) linker and/or $[Fe(Cp)(CO)_2]^+$ moiety, thereby enhancing structural perturbation and thus diminished migration of the DNA target through the agarose gel matrix. Since the ligands coordinated to the Fe(II) centre are all relatively substitution-inert (2 × CO, Cp anion, and a diphenylphosphane) it seems unlikely that the observed EM shift for **10** is due to the Fe(II) and Ru(II) centres cross-linking DNA via simultaneous covalent adduct formation at both metal centres. The fact that the mononuclear Fe(II) complexes **3** and **4** (especially **4**) show no dose-dependent EM shifts when incubated with pUC57 DNA, particularly for the supercoiled form of the plasmid (Figure 5a), confirms the relative inertness of the $[Fe(Cp)(CO)_2(PPh_2R)]^+$ moiety towards ligand exchange and/or DNA binding.

A question worthy of answering is whether the DNA affinity of the compounds might underpin their cytotoxicity. As shown in Table S5 and Figure S70b (Supporting Information), multivariate correlation analysis of the EM shift data, IC_{50} values, and *bis*(phosphane) alkyl chain lengths in compounds **2**, **3** and **5**–**8** for the A2780cis cell line suggests that despite significantly different experimental conditions, there might be a causal relationship between DNA affinity *in vitro* and cytotoxicity in live cell cultures for the present compounds. The relationship is not independent, however, as it varies with the structure of the complex. Going forward, a follow-on study would need to prove that Ru metal can be detected by elemental analysis in the nuclei of A2780cis cells incubated with **5**–**8** to be certain the compounds actually target genomic DNA. Of course, the compounds might also target the histone proteins or other biomolecules in the nucleus and such experiments would need to have a degree of finesse to delineate the actual fate of the compounds in live cells.

Primary Species in Aqueous Solution. Given the likelihood that aquation of **8**–**10** occurs prior to the interaction of these complexes with DNA in the preceding EMSA experiments, the stability of each complex was assessed by UV-visible spectroscopy in the buffer system employed for all electrophoresis measurements to obtain evidence in support of this mechanism. Since compound **10** had a marked impact on the DNA plasmid target (Figure 5), the results for this system are presented and analysed in depth here. From Figure 6a, notable time-dependent changes in the UV-visible spectra of **10** occur at pH 7.6 in 90% aqueous buffer. In the first 10–15 minutes (Phase I) after addition of a DMSO solution of the compound to the aqueous buffer, the UV-visible absorption spectra clearly increase in intensity and the shoulder band at 343 nm (normally assigned to Ru(II) 4d→π* MLCT transitions)[94] becomes somewhat less distinct. The spectra then remain constant in intensity for a considerable length of time (12–60 min), giving rise to a stationary phase, before beginning to decrease in intensity over a period of ~3 h (Phase II), after which the reaction is > 95% complete. This behaviour indicates that there are at least two processes occurring in solution and that their rates differ by several orders of magnitude;

the inset graphs of Figure 6 highlight the kinetics more clearly as plots of the absorbance at 343 nm as a function of time. The fast initial reaction for **10** in aqueous buffer (Phase I) was analysed and is well-fitted by the sigmoidal Gompertz kinetic function,[95] giving the empirical rate constant k_1 = 0.293 ± 0.053 min^{-1}. The data (including the stationary phase from 12–60 min) for the second reaction (Phase II) were well-fitted by the sigmoidal Weibull rate equation (k_2 = 6.18 ± 0.13 × 10^{-3} min^{-1}).[96] The rate constants k_1 and k_2 for **10** thus differ by two orders of magnitude, accounting for the distinct stationary phase evident in the plot of the absorbance data with time. Similar data were recorded for dinuclear **8** and **9** (Figure S75); however, because the two rate constants differed by only one order of magnitude, the stationary phase between the two elementary reaction steps was absent. For **8** and **9**, k_2 measured 7(1) × 10^{-3} and 6(1) × 10^{-3} min^{-1}, respectively. The second step (Phase II) in the reaction is thus identical (within error) for the three dinuclear complexes. In the case of the rate constant for Phase I of the reaction (k_1), **8** and **9** had, within error, equivalent rate constants of 9(2) × 10^{-2} and 7(2) × 10^{-2} min^{-1}, respectively. Reasons for the faster Phase I rate constant for **10** are unclear but may reflect a possible labilizing role for the longer, more flexible bridging diphosphane ligand in this derivative.

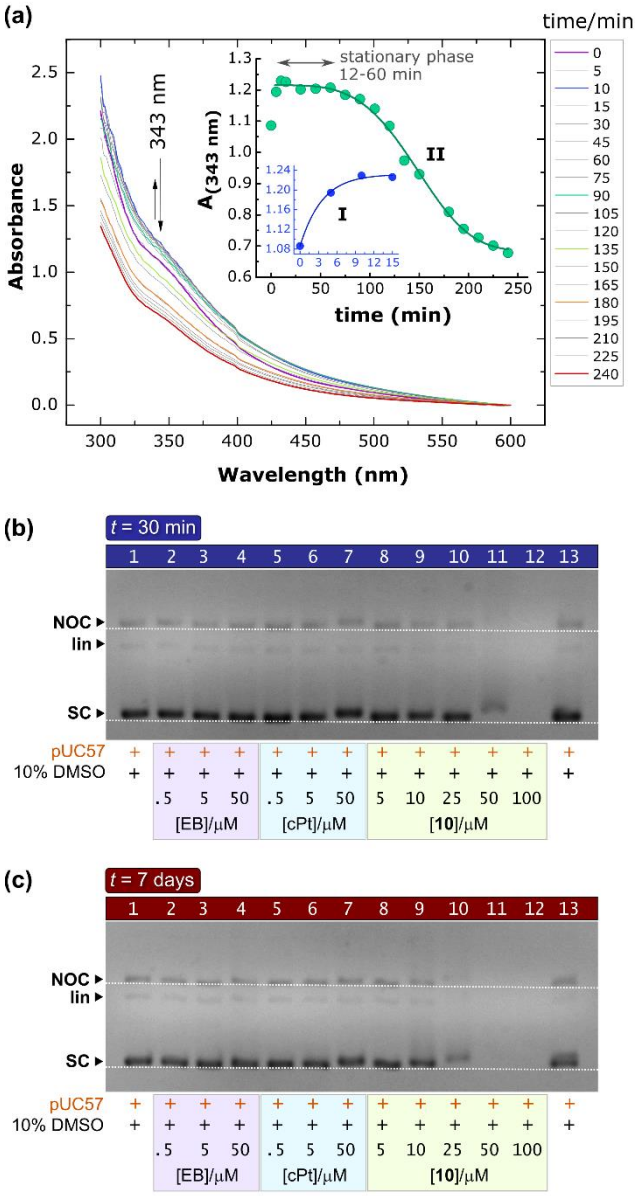

Figure 6. (a) UV-visible spectral changes recorded as a function of time for compound **10** (100 μM) at 37 °C in a TRIS-acetate buffer (40 mM TRIS base, 20 mM sodium acetate, pH 7.6) containing 10% (v/v) DMSO to solubilize the complex. The inset shows a plot of the absorbance measured at 343 nm as a function of time. The fast initial phase (I, $k_1 = 0.293 \pm 0.053$ min^{-1}) precedes a slower second phase (II, $k_2 = 6.18 \pm 0.13 \times 10^{-3}$ min^{-1}). Correlation coefficients (R^2) were 0.989 and 0.995 for the nonlinear regression fits of the first and second phases of the reaction, respectively. (b) Photograph of a 1.25% agarose EMSA gel prepared and run after a 30-minute incubation of varying doses of **10**, ethidium bromide (EB), and cisplatin (cPt) with pUC57 plasmid DNA at 37 °C. (c) Photograph of the analogous gel prepared and run as in Part (b) using the same samples after a storage period of 7 days at 4 ºC.

Because the aquation reactions of di(chloro)ruthenium(II) arene complexes have been thoroughly delineated in the literature using techniques such as ^{35}Cl NMR spectroscopy,[83] the first step in the kinetics of **10** may be assigned to fast chloride/water exchange to yield the mono(aqua) complex **10a** with a total charge of +2, $[RuCl(OH_2)(\eta^6\text{-}p\text{-cymene})(PRPh_2)]^{2+}$, as depicted in Scheme 3 ($PRPh_2$ has R = $[-(CH_2)_5PPh_2-Fe(C_5H_5)(CO)_2]^+$). The second step in the reaction of **10** with water entails substitution

of the remaining chloride ligand in **10a** by water. Concomitant deprotonation of a coordinated aqua ligand yields the mono(hydroxo) species **10b**, $[Ru(OH)(OH_2)(p\text{-cymene})(PRPh_2)]^{2+}$, retaining the +2 charge on the complex (Scheme 3) and substantially altering the absorption spectrum of the complex. Importantly, and despite the differences in solution compositions and structures of the Ru(II) arene derivatives, the rate of aquation of **10** to form the mono(aqua) complex **10a** (k_1 = 4.88(88) × 10^{-3} s^{-1}) matches, within 1σ, that reported by Sadler *et al.* at 37 °C for a 300 μM solution of [RuCl(η^6-biphenyl)(en)]PF_6 (k = 3.95(9) × 10^{-3} s^{-1} in 0.10 M $NaOCl_4$ at pH 6.3; en = ethylenediamine).[97] The rate of formation of **10a** is also similar to that reported by Hartinger *et al.* for the first aquation step of RAPTA (k_1 = 3.33(2) × 10^{-3} s^{-1} at 298 K in 150 mM $NaClO_4$).[98] However, the rate of formation of the hydroxo-aqua complex **10b** was at least two orders of magnitude (500-fold) slower than the formation of $[Ru(OH)(OH_2)(\eta^6\text{-}p\text{-cymene})(pta)]ClO_4$ at 298 K (k_2 = 5.5(2) × 10^{-2} s^{-1} in 150 mM $NaClO_4$).[98]

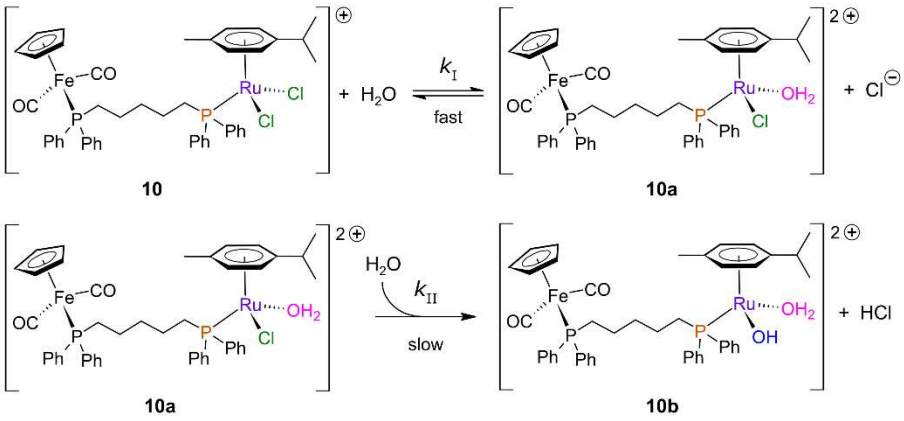

Scheme 3. Postulated two-step aquation of the heterodinuclear [Fe^{II}, Ru^{II}] complex **10** in aqueous buffer at pH 7.6. Based on the time-dependent UV-visible spectra of the system at 37 °C, fast substitution of one chloride ligand coordinated to the Ru(II) ion affords **10a** and precedes slower substitution of the second chloride ligand with concomitant deprotonation of the metal-bound water to form the hydroxo complex **10b**. (The second step would depend on the pH of the solution, warranting a full mechanistic investigation going forward.)

Interestingly, the mononuclear Fe(II) complexes **3** and **5** also underwent aquation in the aqueous buffer employed for the electrophoresis experiments. However, the kinetics were distinctly monophasic for **3** and biphasic for **5** (Figure S76). Compound **4** was, in contrast, unreactive (no time-dependent spectroscopic changes over 4 h). The rate constants k_1 for the first reaction of **3** and **5** is 9(2) × 10^{-2} min^{-1} and 7(1) × 10^{-2} min^{-1}, respectively at 37 °C (Figure S76). Their equivalence within experimental error suggests the first reaction step probably involves nucleophilic attack of Fe(II) by water with substitution of the η^1-*bis*(phosphane) ligand (i.e., hydrolysis of the single Fe–P bond) for both **3** and **5** to give $[Fe(C_5H_5)(CO)_2(OH_2)]^+$ and the free *bis*(phosphane). For reasons that are presently unclear, this reaction is seemingly not possible for **4**. A second reaction follows the first for **5** and has a rate constant

k_2 = 3.4(5) × 10^{-3} min^{-1}. The exact nature of this reaction is unclear at present. However, from the sharpness of the charge-transfer band at 340–350 nm in the UV region, which is largely unshifted in energy, the Fe(Cp)$(CO)_2$ moiety remains intact, suggesting that the second reaction for **5** might involve deprotonation of the aqua ligand or its replacement by acetate from the buffer (Figure S77). Why a similar reaction is not equally feasible for **3** over the same time window is unclear. However, it is possible that the free *bis*(phosphane) ligand participates in the reaction in some way, slowing it to the point of being unobservable for **3** over the data acquisition period. Importantly, the kinetic data indicate that the ligand substitution reactivity order for the mononuclear Fe(II) complexes is **5** > **3** > **4**. This matches the DNA reactivity order for the complexes (Figure 5) and strongly suggests that ligand replacement (metal ion aquation) is the key prerequisite step for DNA binding.

Time-Dependent EMSA Experiments. The rate data in Figure 6a and interpretation of the time-dependent species distribution for **10** are critical to understanding how such complexes interact with plasmid DNA on the timescale of the EMSA experiments, as shown by two EMSA gels recorded for the system at two distinct time points (30 min and 7 days, Figures 6b and 6c). The EMSA gel illustrated in Figure 6b was developed and recorded after incubating (37 °C) pUC57 plasmid DNA with **10** at different concentrations for 30 min in an aqueous buffer at pH 7.6. The kinetics of the system indicate that the mono(aqua) complex **10a** will be the species initially interacting with the DNA target in a reaction that likely involves substitution of water at the Ru(II) centre by a DNA base such as guanine (most likely through coordination to N7 of the purine base)[99] to form covalently-bound Ru–DNA adducts.[100] Once bound, substitution of the second chloride ligand would be entropically favoured and permit dual base binding by the Ru(II) ion. Lane 11 containing 50 μM **10** exhibits the most profound EM shift and both SC and NOC pUC57 plasmid DNA are affected, displaying markedly reduced mobility. The effect is roughly twice as large as that seen for cisplatin at 50 μM (lane 7). Because cisplatin reduces the mobility of both SC and NOC DNA and covalently links pairs of guanine bases on the same or adjacent strands of the DNA target,[87, 88] it is conceivable that **10** interacts with DNA in a similar fashion. (Interestingly, the aqua-chloro species of cisplatin is, like **10a**, dominant at physiological pH.[101]) The larger structure of dinuclear **10**, which comprises a diphosphane linker and $[Fe(Cp)(CO)_2]^+$ moiety, clearly results in a more profound structural perturbation of the DNA target than seen with cisplatin. As noted above, multimodal interaction of **10** with DNA is not impossible with partial or threading intercalation augmenting the primary DNA-binding event (covalent base binding by Ru^{2+}). If this complex mode of DNA binding involves base pairs targeted by ethidium bromide, then steric exclusion of the intercalator dye (used to visualize the DNA) could be dose-dependent and explain why the DNA bands have diminished intensity in Lane 11 and completely vanish in Lane 12 on the gel for **10** (but not cisplatin). It is important to stress that **10** does not induce precipitation of the DNA in the wells, which would reduce the amount of soluble DNA migrating down each lane, so this known phenomenon[84, 102] does not account for the reduced DNA band intensity seen in Lanes 11 and 12. One

additional mechanism could account for the disappearance of the DNA bands on the gel at high doses of **10**, namely, non-specific DNA cleavage to form random, short oligonucleotide fragments. A mixture of low molecular weight DNA fragments would migrate rapidly through the 1.25% agarose gel matrix and out of the gel bed into the buffer in the time taken for the heavy DNA fragments to migrate over the distance that leads to their resolution in Figure 6. Since the reaction buffer used for the EMSA experiment contains DMSO (10% V/V), and DMSO is an efficient hydroxyl radical trap, if dsDNA cleavage is indeed induced by **10**, then it cannot involve hydroxyl radicals. This leaves two possible dsDNA cleavage routes: (i) Ru(II)-mediated binding and activation of dioxygen[103, 104] to form singlet oxygen,[105] superoxide, or peroxide radicals,[106] and/or (ii) phosphodiester bond hydrolysis[107] catalysed by the nucleophilic Ru^{II}–OH group in **10b**. (Photo-induced cleavage of DNA by Ru(II) *p*-cymene complexes is known, occurs via a singlet oxygen-mediated pathway, and gives similar plasmid DNA band profiles to **10** on agarose gels.[108])

Figure 6c shows the same samples as in Figure 6b; however, the agarose gel was loaded, developed, and recorded after storing the reaction solutions at 4 °C for 7 days to gauge the time-dependent changes in the samples. The main difference between the otherwise similar agarose gels of Figures 6c and 6b is that the DNA bands of lanes 10 and 11 (25 and 50 μM **10**, respectively) are weaker in intensity (lane 10) and altogether absent (lane 11). The evidence points to dose-dependent, random cleavage of the high molecular weight DNA species (SC, linear, NOC) into low molecular weight fragments that are undetectable on a 1.25% agarose gel. The reaction(s) continue slowly at 4 °C such that a 50-μM dose of **10** is sufficient over 7 days to completely degrade the DNA while a 25-μM dose of **10** is sufficient to degrade ~50–75% of the DNA. The data also rule out **10** blocking EB uptake (which is fast) by the DNA as the mechanism leading to diminished band intensities at higher compound doses. A deeper investigation of DNA degradation by **10** to elucidate the mechanism involved is seemingly warranted. An important question to answer will be whether the dinuclear complexes themselves dissociate by loss of the bridging diphosphane ligand. As shown by the gels for mononuclear **5** (which lacks the Ru^{2+} ion) in Figure S72, DNA degradation does occur along with DNA binding, events which collectively suggest that ligand exchange at Fe(II) is feasible particularly in the presence of DNA. (In pure DMSO-d_6 over 48 h, the diphosphane ligands remain steadfastly metal-bound; Figures S56–S63.)

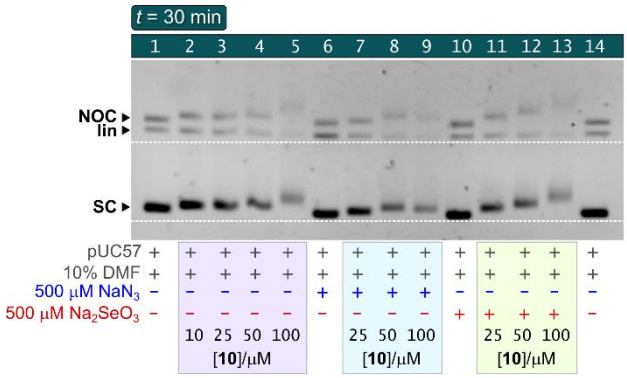

Figure 7. Photograph of a 1.25% agarose EMSA gel prepared and run after a 30-minute incubation of varying doses of **10**, sodium azide (NaN_3), and sodium selenite (Na_2SeO_3) with pUC57 plasmid DNA and DMF (10% V/V to aid compound solubilization) at 37 °C. Sodium azide and sodium selenite trap singlet oxygen and superoxide ions, respectively. Neither reagent reduces the amount of DNA lost due to non-specific cleavage (compare band densities in lanes 5, 9, and 13). However, both salts influence how **10** affects the mobility of the SC and NOC forms of the plasmid.

There are several mechanisms whereby metal complexes may cleave and degrade dsDNA; some are specific to unique sequences, which leads to clean breaks and discrete fragments (earning them the name "chemical nucleases"),[107] while others are non-specific and simply cleave the substrate into a distribution of low MW species. In pH 7 solutions containing triplet state dioxygen ($^3O_2$), redox-active metal ions, and reducing agents, there are four possible species derived from $^3O_2$ that may be involved in the mechanism of DNA degradation: $^1O_2$, $O_2^{\bullet-}$, H_2O_2, and $HO^{\bullet}$ (singlet oxygen, superoxide anion, hydrogen peroxide, and hydroxyl radical).[109] Metal complexes with suitable aromatic ligands (e.g., polypyridines) may act as photosensitizers and promote $^1O_2$ formation,[110] while reduction of metal-bound triplet state dioxygen (M–O_2) can generate superoxide ions via internal 1-electron transfer from the metal ion to the ligand. When M–O_2 undergoes two 1-electron reductions with concomitant protonation, H_2O_2 is produced, and this mechanism usually requires two metal ions or an additional reductant in the system. Homolysis of H_2O_2 (which may be metal-ion dependent) generates highly reactive $HO^{\bullet}$. All the above species may cleave DNA via a multitude of mechanisms.[111]

Given that hydroxyl radicals are neither produced nor responsible for DNA cleavage in the presence of **10** (no radical trapping occurred with 10% added DMSO), we designed an experiment to test whether singlet oxygen (a possible product of photosensitization with Ru(II) complexes) or superoxide ions (theoretically a feasible species produced when Ru^{2+}, or even Fe^{2+}, coordinates $^3O_2$ and reduces it to $O_2^{\bullet-}$) are generated in this system and lead to non-specific DNA cleavage/degradation. As shown in the EMSA gel of Figure 7, neither the addition of excess NaN_3 nor Na_2SeO_3 reduces the DNA degradation that occurs in the presence of 100 μM **10**. The experiment confirms that singlet oxygen and superoxide ions, which are trapped by azide[112, 113] and selenite ions,[114, 115] respectively, are absent and thus do not

account for the loss of DNA in the major bands on the gel. From the marked mobility shifts seen for supercoiled (SC) and nicked open circular (NOC) pUC57 DNA (lanes 5, 9, and 13), **10** interacts significantly with the plasmid target (as noted above), an occurrence evidently enhanced by the considerably higher ionic strength of solutions containing Na_2SeO_3 (lanes 11–13). The subsequent dose-dependent loss of DNA mainly in the SC and NOC bands at higher concentration of the metal complex strongly suggests it is involved in *hydrolytic cleavage* of the dsDNA target to generate random small oligonucleotide fragments.

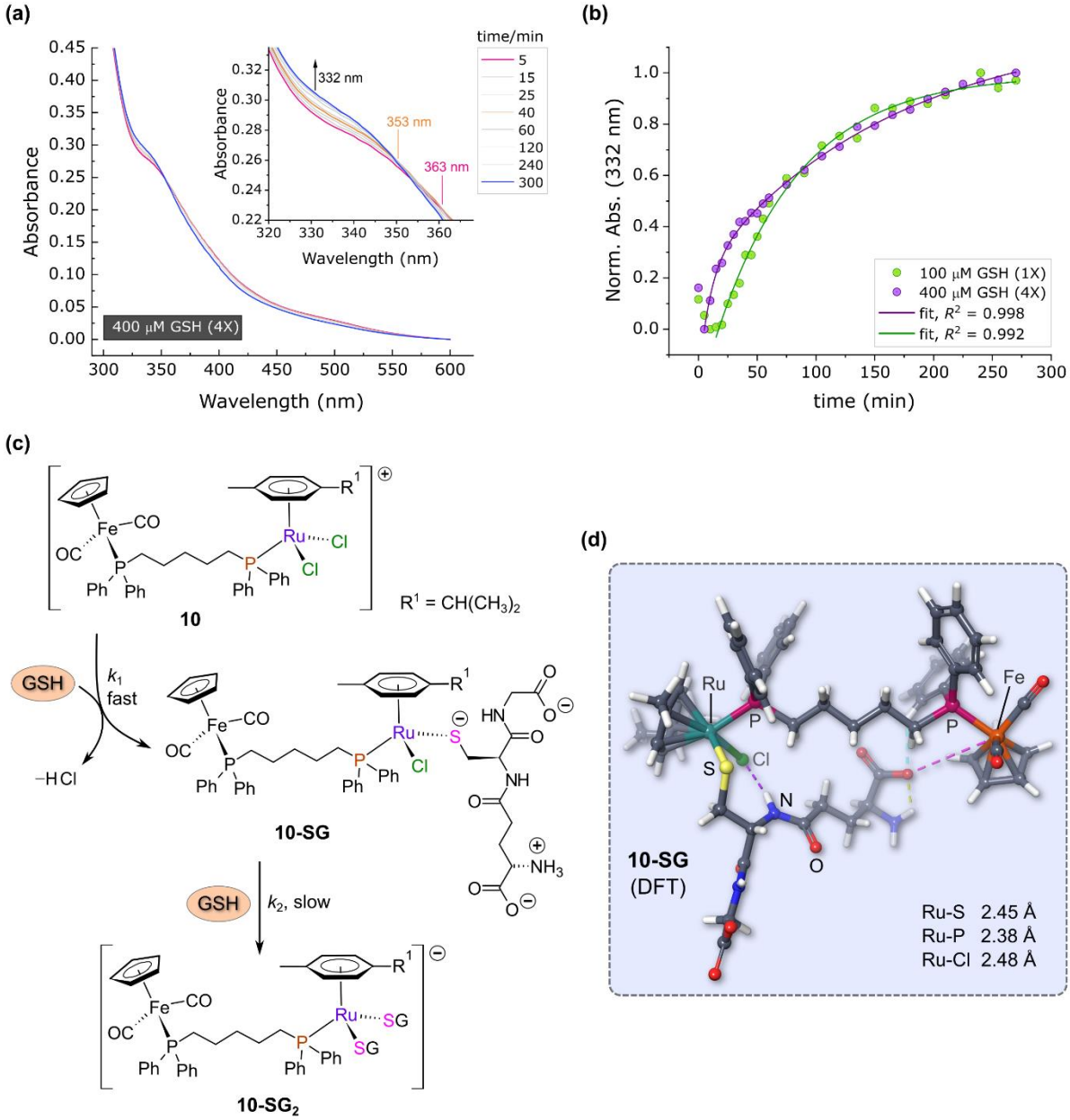

Figure 8. (a) UV-visible spectral changes recorded as a function of time for compound **10** (100 μM) reacting with L-glutathione (GSH, 400 μM) at 37 °C in a 90% (V/V) DMSO/water solution. The inset shows an enlarged view of the spectra measured in the range 320–360 nm. (b) Reaction kinetics as a function of GSH concentration (mole ratios 1X and 4X). The data at 1X are fitted to an empirical first-order growth exponential, $A = A_1 \cdot \exp(-t/t_1) + A_0$, with $k = 1/t_1 = 1.391(83) \times 10^{-2}$ min^{-1}, where t_1 is the decay time constant and A_1 the pre-exponential factor. The data at 4X are fitted to a biphasic (two-step) first-order growth exponential, $A = A_1 \cdot \exp(-t/t_1) + A_2 \cdot \exp(-t/t_2) + A_0$, with $k_1 = 1/t_1 = 1.07(17) \times 10^{-1}$ min^{-1} and $k_2 = 1/t_2 = 6.04(59) \times 10^{-3}$ min^{-1}. (c) Scheme depicting the two reaction steps which match the spectroscopic data when [GSH]/[**10**] ≥ 2. (d) DFT-calculated structure of the mono(GS$^-$) adduct formed with **10**; the structure assignment was based on matching changes in the TD-DFT spectra of **10** and **10-SG** with the experimental spectra (Figure S80). Noncovalent interactions (halogen bond, purple; H-bond, olive green; salt bridge, pink; aromatic C–H···O interaction, cyan) are indicated as dashed lines.

Reactions with glutathione

A common defence mechanism used by tumour cells to limit damage caused by metal ions (and certain drugs) transported into the cell involves thermodynamically favoured metal ion sequestration[116] and/or reduction by glutathione (GSH) as the first step[117] to processing the metal ions for secretion.[118, 119] A high tissue-specific cellular concentration of GSH ranging from *ca.* 1–2 mM is thus typical of tumour cells.[120, 121] Understanding how GSH reacts with putative metallodrug candidates provides insights on their possible fate after cell uptake. The reaction of Ru(II) *p*-cymene complexes with L-glutathione (GSH) does not lead to reduction of the Ru(II) ion; instead stable mono- and polydentate complexes with the metal are formed in which the deprotonated thiol forms a robust Ru–SR bond with the metal ion.[122, 123] This reactivity pattern is most pronounced with chlorido and bromo complexes of the metal such that cations of the type $[RuCl(L)(p\text{-cymene})]^+$, where L is a neutral bidentate *N*,*N*-donor ligand, afford stable adducts with L-glutathione thiolate, $[Ru(SG)(L)(p\text{-cymene})]^+$, in which GS^- substitutes chloride at the metal centre. At very high molar excesses of GSH, the bidentate ligand L in such complexes can be substituted since GS^- is postulated to bind as a tridentate chelate to Ru(II).[122]

The modest spectral changes occurring in the reaction of **10** with GSH (Figure 8a) and the persistence of the MLCT band at ~340 nm, even when the mole ratio [GSH]/[**10**] = 4, confirm that simple step-wise substitution of the chloride ligands by GS^- occurs in **10** with no change in the redox state of the metal ion. The biphasic nature of the substitution kinetics when [GSH]/[**10**] = 4 is highlighted by the isosbestic point established for the initial phase of the reaction at 360 nm up to t = 40 min, after which it blue-shifts to 353 nm for the remainder of the reaction. The d–d transitions responsible for the weak absorption band at ~500 nm are largely unaffected by the substitution reaction because the ligand field strength of Cl^- and RS^- are similar enough that no substantial ligand field perturbation occurs for the low-spin Ru(II) ion. From Figure 8b, the reaction kinetics exhibit the expected dependence on the [GSH]/[**10**] mole ratio. Specifically, when [GSH]/[**10**] = 1, the reaction is monophasic with a first order rate constant k_{1obs} = 1.391(83) × 10^{-2} min^{-1}. When [GSH]/[**10**] ≥ 2, the reaction is clearly biphasic and particularly well-highlighted by the fit of the reaction kinetics at a mole ratio of 4 (4X, Figure 8b), which gives k_{1obs} = 1.07(17) × 10^{-1} min^{-1} and k_{2obs} = 6.04(59) × 10^{-3} min^{-1}. From a plot of the initial rates against [GSH] (Figure S78) and taking into consideration the fact that [GSH] is not >> [**10**], the order of the reaction with respect to [GSH] is 1.15(5) (i.e., ~1) with k_1 = 8.86(19) × 10^{-3} M^{-1} s^{-1} (intercept = 0). This rate constant is similar to that reported for the reaction of $[Ru^{III}(EDTA)(H_2O)]^-$ with GSH (2.6 × 10^{-2} M^{-1} s^{-1} at 25 °C),[124] despite the lower oxidation state of Ru for **10**, higher reaction temperature (37 °C), and presence of 90% DMSO in the present system. This indicates that the first step in the reaction is consistent with expectation, specifically that GSH replaces 1 chlorido ligand at the Ru(II) centre. Because GSH and other thiols normally coordinate to metal ions as the deprotonated thiolate species at neutral pH,[125] we can write the coordination chemistry for the reaction as depicted

schematically in Figure 8c with two distinct GS^- binding steps in which proton loss from the thiol occurs concurrently with Ru–S bond formation. Evidence supporting thiolate coordination to Ru(II) for intermediate species **10-SG** was obtained from TD-DFT simulations (DMSO solvent continuum) of the molecular structure and electronic absorption spectrum of this species (Figure 8d and Figure S80). Specifically, the simulated electronic spectra of **10** and **10-SG** show that the absorbance will increase in the region 275–380 nm and decrease at $\lambda > 380$ nm as **10** reacts with GSH and is converted into **10-SG**. This matches the trend evident in Figure 8a, though the TD-DFT spectra are better-resolved (sharper) and do overestimate the wavelengths of the band maxima and isosbestic point (363 nm) for the first reaction step seen in the experimental spectra by *ca.* 16 nm.

Interestingly, the system is somewhat more complicated than depicted in the scheme because the spectra for the slowest reaction at 1X indicate that an initial process occurs concurrently with the substitution of chloride by GS^-. The absorbance at 332 nm decreases with increasing time until ~15 min into the reaction, at which point a clear reversal (switch) occurs and the absorbance increases in line with the first order exponential curve describing the substitution reaction with GS^-. At 4X, this initial reaction is essentially absent because the reaction between Ru(II) and GS^- is faster. The spectroscopic data confirm that steady solvation of the Ru(II) ion occurs concurrently with the reaction involving the replacement of Cl^- by GS^-.

Ligand exchange in DMSO

A key question to answer is whether ligand exchange reactions in dinuclear complexes such as **10** are restricted to the Ru(II) ion, or can they also occur at the Fe(II) ion? Although it has been suggested that Ru(II) *p*-cymene complexes such as RAPTA do not exchange their chlorido ligands for DMSO or water in solutions containing 90% DMSO,[83] we found that the spectra of the Ru(II) derivative **10** underwent time-dependent changes that were consistent with step-wise substitution of the two chloride ligands in pure DMSO (Figures S73, S74A). The kinetics are distinctly biphasic and the rate constants k_1 and k_2 for **10** measured 0.0882(59) min^{-1} and 0.0093(7) min^{-1}, respectively. This indicates that one of the two chloride ligands of **10** is an order of magnitude more labile than the other towards solvation, in accord with the kinetics observed for aquation of **10** (Scheme 3 and Figure 6). As might be expected, the rate of the first step in the solvation reaction for **10** in pure DMSO is only 30% of that for the reaction in 90% aqueous buffer due to the higher nucleophilicity and lower steric bulk of water. (For Ru^{3+} in complexes such as NAMI-A, $[RuCl_4(imidazole)(S\text{-DMSO})]^-$, water is a better nucleophile than both DMSO and chloride, favouring their substitution at physiological pH.[126]) For compounds **8** and **9**, exchange of the chloride ligands appeared to be orders of magnitude slower or not possible in pure DMSO (Figure S74B). Importantly, the mononuclear Fe(II) complexes **4** and **5** exhibit unchanging electronic spectra in DMSO over a prolonged time period (4h), confirming the exchange-inert nature of the $Fe^{II}(Cp)(CO)_2$ moiety in these derivatives (Figures S74A and S74D). (Mononuclear **3**, in contrast,

was quite unstable in DMSO and rapidly transformed into product(s) in a multiphase reaction whose spectroscopic changes were larger than expected for simple substitution of the dppe ligand by DMSO.)

Returning to the behaviour of **10** towards GSH in 90% DMSO solution and because DMSO exchanges somewhat more slowly with the Ru-bound chloride ions of **10** than competing substitution of chloride by GSH, we are justified in summarizing the dominant substitution reaction(s) for **10** with GSH as depicted in Figure 8c. Finally, and bearing in mind that reactions carried out in DMSO solutions are only approximate models for the solution chemistry of **10** *in vivo* (before and/or after cell uptake), the data at hand clearly confirm that **10** can form one or more adducts with GSH and that the high concentrations of GSH present in cells (typically 1–2 mM)[121] would potentially lead to ligand exchange and/or further reactions with these compounds. Ultimately, the *in vivo* cytotoxicity of the present family of dinuclear *p*-cymene Ru(II) derivatives might be dependent upon both reactive dinuclear and mononuclear species derived from the parent aqua complexes in addition to the aqua complexes themselves and possible adducts formed with glutathione after compound uptake.

MS-ESI for transferrin binding assay

In order to further investigate the potential binding of the heterodinuclear [Fe^{2+}, Ru^{2+}] *bis*(diphenyl-phosphino)alkane complexes with transferrin, we investigated the interaction between transferrin and compound **9** via an MS binding assay. We only performed this assay on one compound since all the dinuclear complexes are structurally analogous. The MS spectra showed an additional set of signals alongside those corresponding to the isotope pattern of the transferrin peak after incubation with compound **9** (Figure 9,10, S81).

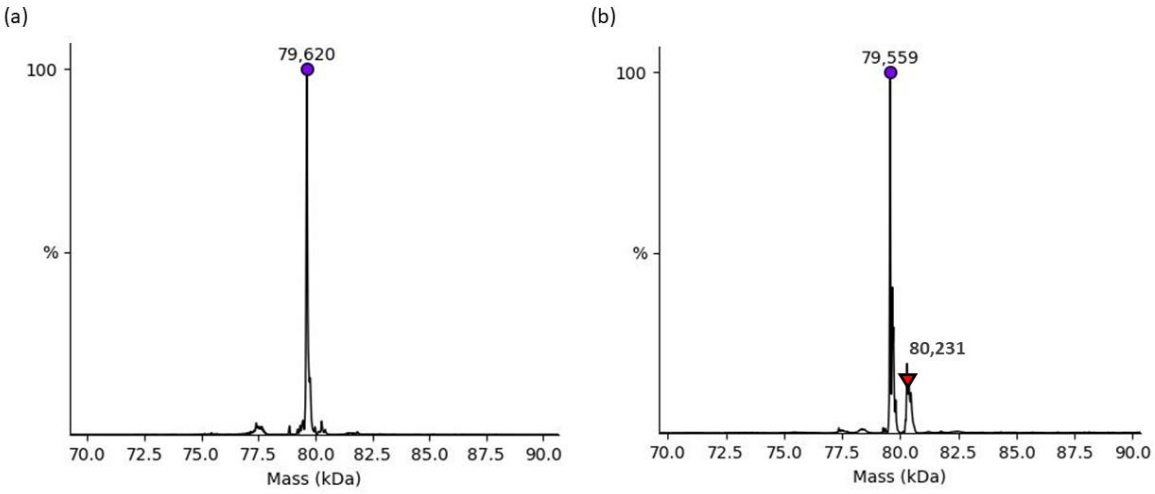

Figure 9. UniDec date of transferrin binding assay. (a) Mass spectrum of transferrin. (b) Mass spectrum of compound **9** and transferrin complex.

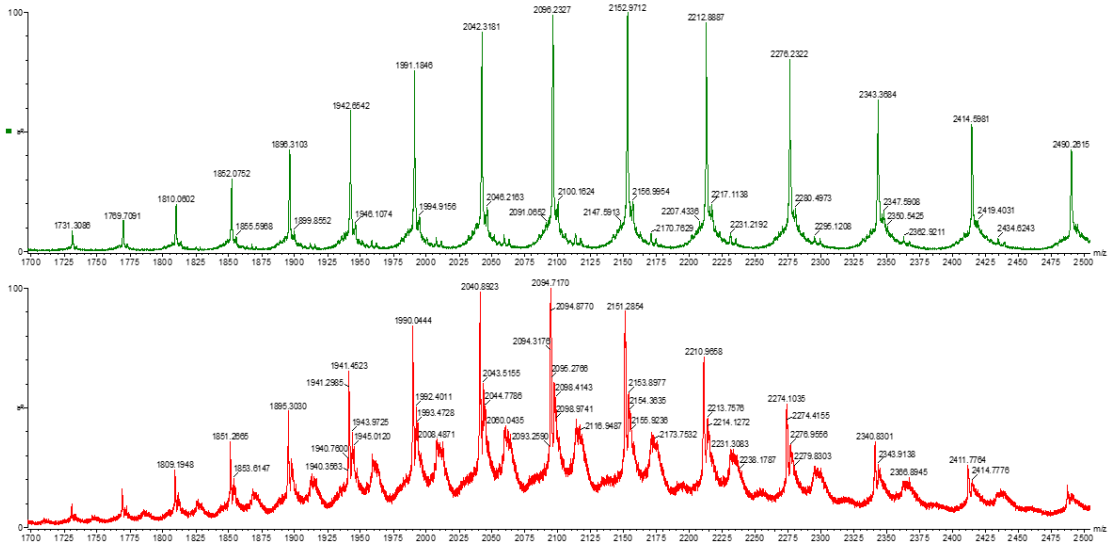

Figure 10. Zoom of transferrin peak (top), incubation with **9** (bottom).

The additional signals alongside those of transferrin in the isotope pattern indicated the possible binding between transferrin and heterodinuclear [Fe^{2+}, Ru^{2+}] *bis*(diphenylphosphino)alkane complex. The mass difference between the transferrin sample and the sample of transferrin incubated with compound was approximately 672 Da. This mass corresponds closely to the fragment ($C_{38}H_{43}P_2Ru^+$ [$Ru(C_{10}H_{14})(\kappa^1$–dppb)(OH)]$^+$). It should be noted that under mass spectrometry conditions fragmentation occurs and so this data indicates potential binding of **9** to transferrin via the Ru moiety with loss of the iron fragment under mass ionization conditions. Nevertheless, this experiment does provide some evidence for*a* potential cellular uptake mechanism which has been reported earlier for mononuclear ruthenium complexes[127] We also explored the interaction of the mononuclear iron complexes (using **4**) with transferrin via a similar assay, but the results were far less satisfactory: no new peaks corresponding to the transferrin plus conjugate were observed as was the case with **9** due to detector limitations.

Summary and Conclusions

Mononuclear iron(II) phosphane complexes bearing tethers of varying length as well as their corresponding dinuclear [Fe^{2+},Ru^{2+}] complexes have been reported. These have been fully characterized by spectral means and density functional theory (DFT) calculations, and their *in vitro* cytotoxicity determined on the cell-lines A2780, A2780cisR and HEK293T. Electrophoretic mobility shift assays (EMSAs) with a plasmid substrate (pUC57) were used to delineate DNA association and DNA cleavage by mononuclear compounds **3**–**5** and dinuclear **8**–**10**. Compound **10** induced the greatest dose-dependent shift in DNA band migration, commensurate with a *possible* nucleobase-binding mechanism. The extent of interaction was dependent on the length of the *bis*(phosphane) linking ligand in the dinuclear derivatives. Only mononuclear **5** interacted with DNA to any significant extent. Kinetic studies of the aquation and solvation (DMSO) reactions of the compounds confirmed that the Ru(II)-bound chloride ligands of **8**–**10** are readily substituted by water in a stepwise reaction, but not by DMSO (compounds **8** and **9**). The mononuclear Fe(II) complexes **3**–**5** behaved differently, with compounds **3** and **5** both undergoing biphasic aquation reactions (**4** was inert). However, only compound **3** underwent ligand exchange in pure DMSO. The results collectively suggest that ligand exchange occurs and is a prerequisite step for DNA association. Notably, the most substitution-labile complexes (**3** and **10**) had the highest cytotoxicity for each compound class in the tumour cell lines studied (A2780 and A2780cis). Time-dependent EMSA data showed that compound **10** was able to cleave dsDNA. The use of radical traps ruled out a mechanism centred on reactive oxygen species ($OH^{\bullet}$, O_2^{-}, and $^1O_2$), pointing to nucleophilic hydrolysis of the phosphodiester bonds of the DNA backbone. Considering the key aquated species formed by **10** at pH 7.6, which contains a putative [$Ru^{II}(OH)(PPh_2R)$(*p*-cymene)(OH_2)]$^+$ moiety, hydrolytic DNA cleavage is *possibly* mediated by the Ru—OH group. Putting the DNA association data into context for **2**, **3** and **5**–**8**, a possible causal relationship between DNA affinity, molecular structure, and cytotoxicity for the A2780cis cell line was found.

Finally, kinetic studies of the reaction between **10** and glutathione (GSH) indicated that the two chloride ligands coordinated to Ru(II) are substituted in stepwise fashion to give a stable adduct (**10-SG$_2$**) in which the Ru(II) ion is probably coordinated to two GS^{-} thiolate ligands. The molecular and electronic structure of the intermediate species, **10-SG**, was determined by TD-DFT simulations. Based on the degree of similitude between the experimental and TD-DFT electronic spectra of **10** and **10-SG**, thiolate coordination to Ru(II) is favourable and accounts for the experimental data. Incubation of the dinuclear complex **9** with transferrin followed by mass spectrometry shows potential binding of the complex to transferrin providing some evidence for a transferrin-mediated uptake mechanism. These complexes represent an interesting new class of potential anti-cancer agents which appear to arrest cell proliferation by DNA binding as a mode of biological action. The *in vitro* cytotoxicity of the bimetallic complexes

are comparable in potency to cisplatin on the A2780cis cell-line and a monotonic increase in cytotoxicity as a function of increased distance between the Fe and Ru centres is observed. Further studies are underway to modulate the ligand sphere at the iron and ruthenium centres on these complexes to further enhance cytotoxic action and to explore other spacers between the metal centres which might enhance stability.

Acknowledgements

We are grateful to Prof. Paul J. Dyson for constructive comments in the preparation of this manuscript and for cytotoxicity testing. BB Thanks Maastricht University, the Faculty of Science and Engineering, and the Maastricht Science Programme for funding and support of this work and the Universiteitsfonds Linburg: SWOL for support. OQM and CAS thank the South African Research Chairs Initiative of the Department of Science and Innovation and National Research Foundation (NRF) of South Africa (SARChI grant number 64799) and the University of the Witwatersrand for generous financial support. OQM thanks the Centre for High Performance Computing (CHPC, Cape Town, RSA; programme CHEM1065) for computational resources.

Abbreviations

- RAPTA-C; dichloro[(1,2,3,4,5,6-η)-1-methyl-4-(1-methylethyl)benzene](1,3,5-triaza-7-phosphatricyclo[3.3.1.13,7]decane-κP7)ruthenium(II)
- NAMI-A; imidazolium *trans*-tetrachloro(*S*-dimethylsulfoxide)imidazoleruthenate(III)
- KP1019; indazolium *trans*-tetrachloro-*bis(*1*H*-indazole)ruthenate(III)
- RM175; [Ru(biphenyl)Cl(en)](PF_6), where en = 1,2-ethylenediamine
- dppm; *bis*(diphenylphosphino)methane
- dppe; *bis*(diphenylphosphino)ethane
- dppp; *bis*(diphenylphosphino)propane
- dppb; *bis*(diphenylphosphino)butane
- DFT; density functional theory

References

1. Siegel, R. L.; Miller, K. D.; Jemal, A., Cancer statistics, 2019. *CA: a cancer journal for clinicians* **2019,** *69* (1), 7-34.
2. Rosenberg, B.; Van Camp, L.; Krigas, T., Inhibition of cell division in Escherichia coli by electrolysis products from a platinum electrode. *Nature* **1965,** *205* (4972), 698-699.

3. O'Dwyer, P. J.; Stevenson, J. P.; Johnson, S. W., Clinical pharmacokinetics and administration of established platinum drugs. *Drugs* **2000,** *59* (4), 19-27.
4. Deo, K. M.; Ang, D. L.; McGhie, B.; Rajamanickam, A.; Dhiman, A.; Khoury, A.; Holland, J.; Bjelosevic, A.; Pages, B.; Gordon, C., Platinum coordination compounds with potent anticancer activity. *Coordination Chemistry Reviews* **2018,** *375*, 148-163.
5. Rosenberg, B.; Vancamp, L.; Trosko, J. E.; Mansour, V. H., Platinum compounds: a new class of potent antitumour agents. *Nature* **1969,** *222* (5191), 385-386.
6. Muhammad, N.; Guo, Z., Metal-based anticancer chemotherapeutic agents. *Current opinion in chemical biology* **2014,** *19*, 144-153.
7. Wong, E.; Giandomenico, C. M., Current status of platinum-based antitumor drugs. *Chemical reviews* **1999,** *99* (9), 2451-2466.
8. Decatris, M.; Sundar, S.; O'byrne, K., Platinum-based chemotherapy in metastatic breast cancer: current status. *Cancer treatment reviews* **2004,** *30* (1), 53-81.
9. Oun, R.; Moussa, Y. E.; Wheate, N. J., The side effects of platinum-based chemotherapy drugs: a review for chemists. *Dalton transactions* **2018,** *47* (19), 6645-6653.
10. Brabec, V.; Kasparkova, J., Modifications of DNA by platinum complexes: relation to resistance of tumors to platinum antitumor drugs. *Drug resistance updates* **2005,** *8* (3), 131-146.
11. Ott, I.; Gust, R., Non platinum metal complexes as anti-cancer drugs. *Archiv der Pharmazie: An International Journal Pharmaceutical and Medicinal Chemistry* **2007,** *340* (3), 117-126.
12. Simović, A. R.; Masnikosa, R.; Bratsos, I.; Alessio, E., Chemistry and reactivity of ruthenium (II) complexes: DNA/protein binding mode and anticancer activity are related to the complex structure. *Coordination Chemistry Reviews* **2019,** *398*, 113011.
13. Schluga, P.; Hartinger, C. G.; Egger, A.; Reisner, E.; Galanski, M.; Jakupec, M. A.; Keppler, B. K., Redox behavior of tumor-inhibiting ruthenium (III) complexes and effects of physiological reductants on their binding to GMP. *Dalton transactions* **2006,** (14), 1796-1802.
14. Antonarakis, E. S.; Emadi, A., Ruthenium-based chemotherapeutics: are they ready for prime time? *Cancer chemotherapy and pharmacology* **2010,** *66* (1), 1-9.
15. Rademaker-Lakhai, J. M.; Van Den Bongard, D.; Pluim, D.; Beijnen, J. H.; Schellens, J. H., A phase I and pharmacological study with imidazolium-trans-DMSO-imidazole-tetrachlororuthenate, a novel ruthenium anticancer agent. *Clinical Cancer Research* **2004,** *10* (11), 3717-3727.
16. Bergamo, A.; Gagliardi, R.; Scarcia, V.; Furlani, A.; Alessio, E.; Mestroni, G.; Sava, G., In vitro cell cycle arrest, in vivo action on solid metastasizing tumors, and host toxicity of the antimetastatic drug NAMI-A and cisplatin. *Journal of Pharmacology and Experimental Therapeutics* **1999,** *289* (1), 559-564.
17. Murray, B. S.; Babak, M. V.; Hartinger, C. G.; Dyson, P. J., The development of RAPTA compounds for the treatment of tumors. *Coordination Chemistry Reviews* **2016,** *306*, 86-114.
18. Inoue, S.; Kawanishi, S., Hydroxyl radical production and human DNA damage induced by ferric nitrilotriacetate and hydrogen peroxide. *Cancer Research* **1987,** *47* (24 Part 1), 6522-6527.
19. Torti, S. V.; Torti, F. M., Iron and cancer: more ore to be mined. *Nature Reviews Cancer* **2013,** *13* (5), 342-355.
20. Hillard, E.; Vessières, A.; Thouin, L.; Jaouen, G.; Amatore, C., Ferrocene-mediated proton-coupled electron transfer in a series of ferrocifen-type breast-cancer drug candidates. *Angewandte Chemie* **2006,** *118* (2), 291-296.
21. Köpf-Maier, P.; Köpf, H.; Neuse, E., Ferricenium complexes: a new type of water-soluble antitumor agent. *Journal of cancer research and clinical oncology* **1984,** *108* (3), 336-340.
22. Alessio, E.; Messori, L., NAMI-A and KP1019/1339, two iconic ruthenium anticancer drug candidates face-to-face: a case story in medicinal inorganic chemistry. *Molecules* **2019,** *24* (10), 1995.
23. Alessio, E.; Mestroni, G.; Bergamo, A.; Sava, G., Ruthenium antimetastatic agents. *Current Topics in Medicinal Chemistry* **2004,** *4* (15), 1525-1535.

24. Hartinger, C. G.; Zorbas-Seifried, S.; Jakupec, M. A.; Kynast, B.; Zorbas, H.; Keppler, B. K., From bench to bedside–preclinical and early clinical development of the anticancer agent indazolium trans-[tetrachlorobis (1H-indazole) ruthenate (III)](KP1019 or FFC14A). *Journal of inorganic biochemistry* **2006,** *100* (5-6), 891-904.
25. Trondl, R.; Heffeter, P.; Kowol, C.; Jakupec, M.; Berger, W.; Keppler, B., NKP-1339, the first ruthenium-based anticancer drug on the edge to clinical application Chem. *Sci* **2014,** *5*, 2925-2932.
26. Heffeter, P.; Atil, B.; Kryeziu, K.; Groza, D.; Koellensperger, G.; Körner, W.; Jungwirth, U.; Mohr, T.; Keppler, B. K.; Berger, W., The ruthenium compound KP1339 potentiates the anticancer activity of sorafenib in vitro and in vivo. *European Journal of Cancer* **2013,** *49* (15), 3366-3375.
27. Alessio, E.; Messori, L., The deceptively similar ruthenium (III) drug candidates KP1019 and NAMI-A have different actions. what did we learn in the past 30 years. *Metallo-Drugs: Development and Action of Anticancer Agents* **2018,** *18* (141), 9783110470734-005.
28. Gasser, G.; Ott, I.; Metzler-Nolte, N., Organometallic anticancer compounds. *Journal of medicinal chemistry* **2011,** *54* (1), 3-25.
29. Renfrew, A., Ruthenium (II) arene compounds as versatile anticancer agents. *CHIMIA International Journal for Chemistry* **2009,** *63* (4), 217-219.
30. Dougan, S. J.; Sadler, P. J., The design of organometallic ruthenium arene anticancer agents. *CHIMIA International Journal for Chemistry* **2007,** *61* (11), 704-715.
31. Yan, Y. K.; Melchart, M.; Habtemariam, A.; Sadler, P. J., Organometallic chemistry, biology and medicine: ruthenium arene anticancer complexes. *Chemical communications* **2005,** (38), 4764-4776.
32. Scolaro, C.; Bergamo, A.; Brescacin, L.; Delfino, R.; Cocchietto, M.; Laurenczy, G.; Geldbach, T. J.; Sava, G.; Dyson, P. J., In vitro and in vivo evaluation of ruthenium (II)− arene PTA complexes. *Journal of medicinal chemistry* **2005,** *48* (12), 4161-4171.
33. Habtemariam, A.; Melchart, M.; Fernández, R.; Parsons, S.; Oswald, I. D.; Parkin, A.; Fabbiani, F. P.; Davidson, J. E.; Dawson, A.; Aird, R. E., Structure− activity relationships for cytotoxic ruthenium (II) arene complexes containing N, N-, N, O-, and O, O-chelating ligands. *Journal of medicinal chemistry* **2006,** *49* (23), 6858-6868.
34. Aird, R.; Cummings, J.; Ritchie, A.; Muir, M.; Morris, R.; Chen, H.; Sadler, P.; Jodrell, D., In vitro and in vivo activity and cross resistance profiles of novel ruthenium (II) organometallic arene complexes in human ovarian cancer. *British journal of cancer* **2002,** *86* (10), 1652-1657.
35. Pitchaimani, J.; Raja, M. R. C.; Sujatha, S.; Mahapatra, S. K.; Moon, D.; Anthony, S. P.; Madhu, V., Arene ruthenium (II) complexes with chalcone, aminoantipyrine and aminopyrimidine based ligands: synthesis, structure and preliminary evaluation of anti-leukemia activity. *RSC advances* **2016,** *6* (93), 90982-90992.
36. Novakova, O.; Chen, H.; Vrana, O.; Rodger, A.; Sadler, P. J.; Brabec, V., DNA interactions of monofunctional organometallic ruthenium (II) antitumor complexes in cell-free media. *Biochemistry* **2003,** *42* (39), 11544-11554.
37. Pettinari, R.; Marchetti, F.; Condello, F.; Pettinari, C.; Lupidi, G.; Scopelliti, R.; Mukhopadhyay, S.; Riedel, T.; Dyson, P. J., Ruthenium (II)–arene RAPTA type complexes containing curcumin and bisdemethoxycurcumin display potent and selective anticancer activity. *Organometallics* **2014,** *33* (14), 3709-3715.
38. Weiss, A.; Berndsen, R. H.; Dubois, M.; Müller, C.; Schibli, R.; Griffioen, A. W.; Dyson, P. J.; Nowak-Sliwinska, P., In vivo anti-tumor activity of the organometallic ruthenium (II)-arene complex [Ru (η 6-p-cymene) Cl 2 (pta)](RAPTA-C) in human ovarian and colorectal carcinomas. *Chemical Science* **2014,** *5* (12), 4742-4748.
39. Bergamo, A.; Gaiddon, C.; Schellens, J.; Beijnen, J.; Sava, G., Approaching tumour therapy beyond platinum drugs: status of the art and perspectives of ruthenium drug candidates. *Journal of inorganic biochemistry* **2012,** *106* (1), 90-99.

40. Chatterjee, S.; Kundu, S.; Bhattacharyya, A.; Hartinger, C. G.; Dyson, P. J., The ruthenium (II)–arene compound RAPTA-C induces apoptosis in EAC cells through mitochondrial and p53–JNK pathways. *JBIC Journal of Biological Inorganic Chemistry* **2008,** *13* (7), 1149-1155.
41. Bergamo, A.; Masi, A.; Peacock, A.; Habtemariam, A.; Sadler, P. J.; Sava, G., In vivo tumour and metastasis reduction and in vitro effects on invasion assays of the ruthenium RM175 and osmium AFAP51 organometallics in the mammary cancer model. *Journal of inorganic biochemistry* **2010,** *104* (1), 79-86.
42. Alessio, E., Thirty years of the drug candidate nami-a and the myths in the field of ruthenium anticancer compounds: a personal perspective. *European Journal of Inorganic Chemistry* **2017,** *2017* (12), 1549-1560.
43. Bytzek, A. K.; Koellensperger, G.; Keppler, B. K.; Hartinger, C. G., Biodistribution of the novel anticancer drug sodium trans-[tetrachloridobis (1H-indazole) ruthenate (III)] KP-1339/IT139 in nude BALB/c mice and implications on its mode of action. *Journal of inorganic biochemistry* **2016,** *160*, 250-255.
44. Groessl, M.; Hartinger, C. G.; Polec-Pawlak, K.; Jarosz, M.; Keppler, B. K., Capillary electrophoresis hyphenated to inductively coupled plasma-mass spectrometry: A novel approach for the analysis of anticancer metallodrugs in human serum and plasma. *Electrophoresis* **2008,** *29* (10), 2224-2232.
45. Sulyok, M.; Hann, S.; Hartinger, C.; Keppler, B.; Stingeder, G.; Koellensperger, G., Two dimensional separation schemes for investigation of the interaction of an anticancer ruthenium (III) compound with plasma proteins. *Journal of Analytical Atomic Spectrometry* **2005,** *20* (9), 856-863.
46. Timerbaev, A. R.; Hartinger, C. G.; Aleksenko, S. S.; Keppler, B. K., Interactions of antitumor metallodrugs with serum proteins: advances in characterization using modern analytical methodology. *Chemical reviews* **2006,** *106* (6), 2224-2248.
47. Sullivan, M. P.; Holtkamp, H. U.; Hartinger, C. G., Antitumor Metallodrugs That Target Proteins. *Met. Ions Life Sci* **2018,** *18*, 351-386.
48. Scott, B. J.; Bradwell, A. R., Identification of the serum binding proteins for iron, zinc, cadmium, nickel, and calcium. *Clinical chemistry* **1983,** *29* (4), 629-633.
49. Steegmann-Olmedillas, J. L., The role of iron in tumour cell proliferation. *Clinical and Translational Oncology* **2011,** *13* (2), 71-76.
50. Thévenod, F., Iron and its role in cancer defense: a double-edged sword. *Met Ions Life Sci* **2018,** *18*, 437-467.
51. Macedo, M. F.; Sousa, M. d., Transferrin and the transferrin receptor: of magic bullets and other concerns. *Inflammation & Allergy-Drug Targets (Formerly Current Drug Targets-Inflammation & Allergy)(Discontinued)* **2008,** *7* (1), 41-52.
52. Fernández-Gallardo, J.; Elie, B. T.; Sanaú, M.; Contel, M., Versatile synthesis of cationic N-heterocyclic carbene–gold (I) complexes containing a second ancillary ligand. Design of heterobimetallic ruthenium–gold anticancer agents. *Chemical Communications* **2016,** *52* (15), 3155-3158.
53. Serra, D.; Abboud, K. A.; Hilliard, C. R.; McElwee-White, L., Electronic Interactions in Iron- and Ruthenium-Containing Heterobimetallic Complexes: Structural and Spectroscopic Investigations. *ORGANOMETALLICS* **2007,** *26* (13), 3085-3093.
54. Massai, L.; Fernández-Gallardo, J.; Guerri, A.; Arcangeli, A.; Pillozzi, S.; Contel, M.; Messori, L., Design, synthesis and characterisation of new chimeric ruthenium (II)–gold (I) complexes as improved cytotoxic agents. *Dalton Transactions* **2015,** *44* (24), 11067-11076.
55. Jacobsen, G. B.; Shaw, B. L.; Thornton-Pett, M., Rhodium(I)–iron(0) carbonyl complexes containing one bridging Ph2PCH2PPh2 ligand, including the formation of a tetranuclear cluster from a heterobimetallic precursor: crystal structures of [(OC)4Fe(μ-Ph2PCH2PPh2)RhCl(CO)] and [Fe2Rh2(μ-Ph2PCH2PPh2)2(CO)8]. *Journal of the Chemical Society, Dalton Transactions* **1987,** (11), 2751-2755.

56. Odachowski, M.; Marschner, C.; Blom, B., A review on 1, 1-bis (diphenylphosphino) methane bridged homo-and heterobimetallic complexes for anticancer applications: Synthesis, structure, and cytotoxicity. *European Journal of Medicinal Chemistry* **2020**, 112613.
57. McCleverty, J. A.; Ward, M. D., The role of bridging ligands in controlling electronic and magnetic properties in polynuclear complexes. *Accounts of chemical research* **1998,** *31* (12), 842-851.
58. Tolman, C. A., Steric effects of phosphorus ligands in organometallic chemistry and homogeneous catalysis. *Chemical Reviews* **1977,** *77* (3), 313-348.
59. Puddephatt, R. J., Chemistry of bis (diphenylphosphino) methane. *Chemical Society Reviews* **1983,** *12* (2), 99-127.
60. Hughes, A. N., Bis (diphenylphosphino) methane in Organometallic Synthesis: New Applications. **1992**.
61. Aldeghi, N.; Romano, D.; Marschner, C.; Biswas, S.; Chakraborty, S.; Prince, S.; Ngubane, S.; Blom, B., Facile entry to germanate and stannate complexes [(η6-arene)RuCl(η2-dppm)]+[ECl3]- (E = Ge, Sn) as potent anti-cancer agents. *Journal of Organometallic Chemistry* **2020,** *916*, 121214.
62. Renier, O.; Deacon-Price, C.; Peters, J. E.; Nurekeyeva, K.; Russon, C.; Dyson, S.; Ngubane, S.; Baumgartner, J.; Dyson, P. J.; Riedel, T., Synthesis and in vitro (anticancer) evaluation of η6-arene ruthenium complexes bearing stannyl ligands. *Inorganics* **2017,** *5* (3), 44.
63. Deacon-Price, C.; Romano, D.; Riedel, T.; Dyson, P. J.; Blom, B., Synthesis, characterisation and cytotoxicity studies of ruthenium arene complexes bearing trichlorogermyl ligands. *Inorganica Chimica Acta* **2019,** *484*, 513-520.
64. Herry, B.; Roufosse, B.; Borzova, M.; Reifenstahl, T.; Collins, T.; Benamrane, A.; Weggelaar, J.; Correia, M. C.; Blom, B.; Romano, D.; Baumgartner, J.; Batchelor, L. K.; Dyson, P. J., Heterobimetallic Ru(μ-dppm)Fe and homobimetallic Ru(μ-dppm)Ru complexes as potential anti-cancer agents. *Journal of Organometallic Chemistry* **2019,** *901*.
65. BenYosef, D.; Romano, D.; Hadiji, M.; Dyson, P. J.; Blom, B., Facile synthesis of heterobimetallic [FeII(μ-diphosphine)RuII] and homobimetallic [FeII(μ-diphosphine)FeII] complexes and their in vitro cytotoxic activity on cisplatin-resistant cancer cells. *Inorganica Chimica Acta* **2020,** *510*.
66. Connelly, N. G.; Geiger, W. E., Chemical redox agents for organometallic chemistry. *Chemical Reviews* **1996,** *96* (2), 877-910.
67. Schumann, H., Alkylidenverbrückte diphosphane und dichlalkogenodiphosphorane als liganden in kationischen cyclopentadienyleisencarbonyl-komplexen. *Journal of organometallic chemistry* **1987,** *320* (2), 145-162.
68. (a)Frisch, M.; Clemente, F., Gaussian 09, Revision A. 01, MJ Frisch, GW Trucks, HB Schlegel, GE Scuseria, MA Robb, JR Cheeseman, G. *Scalmani, V. Barone, B. Mennucci, GA Petersson, H. Nakatsuji, M. Caricato, X. Li, HP Hratchian, AF Izmaylov, J. Bloino, G. Zhe* **2009**. (b) A.D. Becke, J.Chem.Phys. 98 (1993) 5648-5652. (c) C. Lee, W. Yang, R.G. Parr, Phys. Rev. B 37 (1988) 785-789. (d) S.H. Vosko, L. Wilk, M. Nusair, Can. J. Phys. 58 (1980) 1200-1211. (e) P.J. Stephens, F.J. Devlin, C.F. Chabalowski, M.J. Frisch, J.Phys.Chem. 98 (1994) 11623-11627. (f)

69. Yanai, T.; Tew, D. P.; Handy, N. C., A new hybrid exchange–correlation functional using the Coulomb-attenuating method (CAM-B3LYP). *Chemical physics letters* **2004,** *393* (1-3), 51-57.
70. Fuentealba, P.; Preuss, H.; Stoll, H.; Von Szentpaly, L., A proper account of core-polarization with pseudopotentials: single valence-electron alkali compounds. *Chemical Physics Letters* **1982,** *89* (5), 418-422.
71. Cossi, M.; Barone, V.; Cammi, R.; Tomasi, J., Ab initio study of solvated molecules: a new implementation of the polarizable continuum model. *Chemical Physics Letters* **1996,** *255* (4-6), 327-335.
72. Grimme, S.; Ehrlich, S.; Goerigk, L., Effect of the damping function in dispersion corrected density functional theory. *Journal of computational chemistry* **2011,** *32* (7), 1456-1465.

73. Scalmani, G.; Frisch, M. J.; Mennucci, B.; Tomasi, J.; Cammi, R.; Barone, V., Geometries and properties of excited states in the gas phase and in solution: Theory and application of a time-dependent density functional theory polarizable continuum model. *The Journal of chemical physics* **2006,** *124* (9), 094107.
74. Isaacs, E.; Graham, W., Synthesis and Spectra of Cationic Bis (tertiary phosphine) derivatives of cycloheptatrienyliummolybdenum and cyclopentadienyliron complexes. *Journal of Organometallic Chemistry* **1976,** *120* (3), 407-421.
75. Hildebrandt, B. r.; Frank, W.; Ganter, C., A Cationic N-Heterocyclic Carbene with an Organometallic Backbone: Synthesis and Reactivity. *Organometallics* **2011,** *30* (13), 3483-3486.
76. Prakash, O.; Sharma, K. N.; Joshi, H.; Gupta, P. L.; Singh, A. K., Half sandwich complexes of chalcogenated pyridine based bi-(N, S/Se) and terdentate (N, S/Se, N) ligands with (η 6-benzene) ruthenium (ii): synthesis, structure and catalysis of transfer hydrogenation of ketones and oxidation of alcohols. *Dalton Transactions* **2013,** *42* (24), 8736-8747.
77. Gemel, C.; Sapunov, V. N.; Mereiter, K.; Ferencic, M.; Schmid, R.; Kirchner, K., Cationic 16-electron half-sandwich ruthenium complexes containing asymmetric diamines: understanding the stability and reactivity of coordinatively unsaturated two-legged piano stool complexes. *Inorganica chimica acta* **1999,** *286* (1), 114-120.
78. van der Westhuizen, D.; Bezuidenhout, D. I.; Munro, O. Q., Cancer molecular biology and strategies for the design of cytotoxic gold (I) and gold (III) complexes: a tutorial review. *Dalton Transactions* **2021**, *50* (47), 17413-17437.
79. Hall, J. P.; O'Sullivan, K.; Naseer, A.; Smith, J. A.; Kelly, J. M.; Cardin, C. J., Structure determination of an intercalating ruthenium dipyridophenazine complex which kinks DNA by semiintercalation of a tetraazaphenanthrene ligand. *Proceedings of the National Academy of Sciences* **2011,** *108* (43), 17610.
80. Seručnik, M.; Podlipnik, C. r.; Hribar-Lee, B., DNA–Polyelectrolyte Complexation Study: The Effect of Polyion Charge Density and Chemical Nature of the Counterions. *The Journal of Physical Chemistry B* **2018,** *122* (21), 5381-5388.
81. Rocha, M.; Cavalcante, A.; Silva, R.; Ramos, E., On the effects of intercalators in DNA condensation: a force spectroscopy and gel electrophoresis study. *The Journal of Physical Chemistry B* **2014,** *118* (18), 4832-4839.
82. Stebler-Roethlisberger, M.; Hummel, W.; Pittet, P. A.; Buergi, H. B.; Ludi, A.; Merbach, A. E., Triaqua (benzene) ruthenium (II) and triaqua (benzene) osmium (II): synthesis, molecular structure, and water-exchange kinetics. *Inorganic Chemistry* **1988,** *27* (8), 1358-1363.
83. Biancalana, L.; Zacchini, S.; Ferri, N.; Lupo, M. G.; Pampaloni, G.; Marchetti, F., Tuning the cytotoxicity of ruthenium (II) para-cymene complexes by mono-substitution at a triphenylphosphine/phenoxydiphenylphosphine ligand. *Dalton Transactions* **2017,** *46* (47), 16589-16604.
84. Snelders, D. J.; Casini, A.; Edafe, F.; van Koten, G.; Gebbink, R. J. K.; Dyson, P. J., Ruthenium (II) arene complexes with oligocationic triarylphosphine ligands: Synthesis, DNA interactions and in vitro properties. *Journal of Organometallic Chemistry* **2011,** *696* (5), 1108-1116.
85. Ratanaphan, A.; Temboot, P.; Dyson, P. J., In vitro Ruthenation of Human Breast Cancer Suppressor Gene 1 (BRCA1) by the Antimetastasis Compound RAPTA-C and Its Analogue CarboRAPTA-C. *Chemistry & Biodiversity* **2010,** *7* (5), 1290-1302.
86. Ang, W. H.; Casini, A.; Sava, G.; Dyson, P. J., Organometallic ruthenium-based antitumor compounds with novel modes of action. *Journal of Organometallic Chemistry* **2011,** *696* (5), 989-998.
87. Gelasco, A.; Lippard, S. J., NMR solution structure of a DNA dodecamer duplex containing a cis-diammineplatinum (II) d (GpG) intrastrand cross-link, the major adduct of the anticancer drug cisplatin. *Biochemistry* **1998,** *37* (26), 9230-9239.
88. Todd, R. C.; Lippard, S. J., Structure of duplex DNA containing the cisplatin 1, 2-{Pt (NH3) 2} 2+-d (GpG) cross-link at 1.77 Å resolution. *Journal of inorganic biochemistry* **2010,** *104* (9), 902-908.

89. Busto, N.; Valladolid, J.; Martínez-Alonso, M.; Lozano, H. c. J.; Jalon, F. A.; Manzano, B. R.; Rodríguez, A.; Carrion, M. C.; Biver, T.; Leal, J. M., Anticancer activity and DNA binding of a bifunctional Ru (II) arene aqua-complex with the 2, 4-diamino-6-(2-pyridyl)-1, 3, 5-triazine ligand. *Inorganic Chemistry* **2013,** *52* (17), 9962-9974.
90. Dorcier, A.; Hartinger, C. G.; Scopelliti, R.; Fish, R. H.; Keppler, B. K.; Dyson, P. J., Studies on the reactivity of organometallic Ru–, Rh–and Os–pta complexes with DNA model compounds. *Journal of Inorganic Biochemistry* **2008,** *102* (5-6), 1066-1076.
91. Dorcier, A.; Dyson, P. J.; Gossens, C.; Rothlisberger, U.; Scopelliti, R.; Tavernelli, I., Binding of organometallic ruthenium (II) and osmium (II) complexes to an oligonucleotide: a combined mass spectrometric and theoretical study. *Organometallics* **2005,** *24* (9), 2114-2123.
92. Lovejoy, K. S.; Todd, R. C.; Zhang, S.; McCormick, M. S.; D'Aquino, J. A.; Reardon, J. T.; Sancar, A.; Giacomini, K. M.; Lippard, S. J., cis-Diammine (pyridine) chloroplatinum (II), a monofunctional platinum (II) antitumor agent: Uptake, structure, function, and prospects. *Proceedings of the National Academy of Sciences* **2008,** *105* (26), 8902-8907.
93. Allardyce, C. S.; Dyson, P. J.; Ellis, D. J.; Heath, S. L., [Ru (η6-p-cymene) Cl2 (pta)](pta= 1, 3, 5-triaza-7-phosphatricyclo-[3.3. 1.1] decane): a water soluble compound that exhibits pH dependent DNA binding providing selectivity for diseased cells. *Chemical Communications* **2001,** (15), 1396-1397.
94. Lenis-Rojas, O. A.; Robalo, M. P.; Tomaz, A. I.; Fernandes, A. R.; Roma-Rodrigues, C.; Teixeira, R. G.; Marques, F.; Folgueira, M.; Yáñez, J.; Gonzalez, A. A., Half-Sandwich Ru (p-cymene) Compounds with Diphosphanes: In Vitro and In Vivo Evaluation As Potential Anticancer Metallodrugs. *Inorganic Chemistry* **2021,** *60* (5), 2914-2930.
95. Yin, X.; Goudriaan, J.; Lantinga, E. A.; Vos, J.; Spiertz, H. J., A flexible sigmoid function of determinate growth. *Annals of botany* **2003,** *91* (3), 361-371.
96. Rocha, J. L.; Aleixo, S. M., An extension of Gompertzian growth dynamics: Weibull and Fréchet models. *Mathematical Biosciences & Engineering* **2013,** *10* (2), 379.
97. Wang, F.; Chen, H.; Parsons, S.; Oswald, I. D.; Davidson, J. E.; Sadler, P. J., Kinetics of Aquation and Anation of Ruthenium (II) Arene Anticancer Complexes, Acidity and X-ray Structures of Aqua Adducts. *Chemistry–A European Journal* **2003,** *9* (23), 5810-5820.
98. Scolaro, C.; Hartinger, C. G.; Allardyce, C. S.; Keppler, B. K.; Dyson, P. J., Hydrolysis study of the bifunctional antitumour compound RAPTA-C,[Ru (η6-p-cymene) Cl2 (pta)]. *Journal of inorganic biochemistry* **2008,** *102* (9), 1743-1748.
99. Chen, H.; Parkinson, J. A.; Parsons, S.; Coxall, R. A.; Gould, R. O.; Sadler, P. J., Organometallic ruthenium (II) diamine anticancer complexes: arene-nucleobase stacking and stereospecific hydrogen-bonding in guanine adducts. *Journal of the American Chemical Society* **2002,** *124* (12), 3064-3082.
100. Liu, H. K.; Wang, F.; Parkinson, J. A.; Bella, J.; Sadler, P. J., Ruthenation of duplex and single-stranded d (CGGCCG) by organometallic anticancer complexes. *Chemistry–A European Journal* **2006,** *12* (23), 6151-6165.
101. Davies, M. S.; Berners-Price, S. J.; Hambley, T. W., Slowing of cisplatin aquation in the presence of DNA but not in the presence of phosphate: improved understanding of sequence selectivity and the roles of monoaquated and diaquated species in the binding of cisplatin to DNA. *Inorganic chemistry* **2000,** *39* (25), 5603-5613.
102. Akerman, K. J.; Fagenson, A. M.; Cyril, V.; Taylor, M.; Muller, M. T.; Akerman, M. P.; Munro, O. Q., Gold (III) macrocycles: nucleotide-specific unconventional catalytic inhibitors of human topoisomerase I. *Journal of the American Chemical Society* **2014,** *136* (15), 5670-5682.
103. Stark, M. J.; Shaw, M. J.; Fadamin, A.; Rath, N. P.; Bauer, E. B., Synthesis, structural characterization and catalytic activity of indenyl complexes of ruthenium bearing fluorinated phosphine ligands. *Journal of Organometallic Chemistry* **2017,** *847*, 41-53.
104. Albertin, G.; Antoniutti, S.; Bortoluzzi, M.; Castro, J.; Ferraro, V., Preparation and reactivity of half-sandwich dioxygen complexes of ruthenium. *Dalton Transactions* **2018,** *47* (27), 9173-9184.

105. Shao, J.; Yan, Z.-Y.; Tang, M.; Huang, C.-H.; Sheng, Z.-G.; Chen, J.; Shao, B.; Zhu, B.-Z., Potent oxidation of DNA by Ru (ii) tri (polypyridyl) complexes under visible light irradiation via a singlet oxygen-mediated mechanism. *Inorganic Chemistry Frontiers* **2021,** *8* (14), 3421-3432.
106. Mari, C.; Pierroz, V.; Ferrari, S.; Gasser, G., Combination of Ru (II) complexes and light: new frontiers in cancer therapy. *Chemical science* **2015,** *6* (5), 2660-2686.
107. Sigman, D. S.; Mazumder, A.; Perrin, D. M., Chemical nucleases. *Chemical Reviews* **1993,** *93* (6), 2295-2316.
108. Gopalakrishnan, D.; Srinath, S.; Baskar, B.; Bhuvanesh, N. S.; Ganeshpandian, M., Biological and catalytic evaluation of Ru (II)-p-cymene complexes of Schiff base ligands: Impact of ligand appended moiety on photo-induced DNA and protein cleavage, cytotoxicity and C-H activation. *Applied Organometallic Chemistry* **2019,** *33* (3), e4756.
109. Szaciłowski, K.; Macyk, W.; Drzewiecka-Matuszek, A.; Brindell, M.; Stochel, G., Bioinorganic photochemistry: frontiers and mechanisms. *Chemical reviews* **2005,** *105* (6), 2647-2694.
110. Stacey, O. J.; Pope, S. J., New avenues in the design and potential application of metal complexes for photodynamic therapy. *Rsc Advances* **2013,** *3* (48), 25550-25564.
111. Griffith, C.; Dayoub, A. S.; Jaranatne, T.; Alatrash, N.; Mohamedi, A.; Abayan, K.; Breitbach, Z. S.; Armstrong, D. W.; MacDonnell, F. M., Cellular and cell-free studies of catalytic DNA cleavage by ruthenium polypyridyl complexes containing redox-active intercalating ligands. *Chemical Science* **2017,** *8* (5), 3726-3740.
112. Yamamoto, K.; Inoue, S.; Yamazaki, A.; Yoshinaga, T.; Kawanishi, S., Site-specific DNA damage induced by cobalt (II) ion and hydrogen peroxide: role of singlet oxygen. *Chemical research in toxicology* **1989,** *2* (4), 234-239.
113. Miyoshi, N.; Tomita, G., Quenching of singlet oxygen by sodium azide in reversed micellar systems. *Zeitschrift für Naturforschung B* **1979,** *34* (2), 339-343.
114. Ma, W.; Jing, L.; Valladares, A.; Mehta, S. L.; Wang, Z.; Li, P. A.; Bang, J. J., Silver nanoparticle exposure induced mitochondrial stress, caspase-3 activation and cell death: amelioration by sodium selenite. *International journal of biological sciences* **2015,** *11* (8), 860.
115. Feroci, G.; Fini, A., Study of the antioxidant effect of several selenium and sulphur compounds. *Journal of trace elements in medicine and biology* **1998,** *12* (2), 96-100.
116. Krezel, A.; Bal, W., Coordination chemistry of glutathione. *Acta Biochimica Polonica* **1999,** *46* (3), 567-580.
117. Hayes, J. D.; McLellan, L. I., Glutathione and glutathione-dependent enzymes represent a co-ordinately regulated defence against oxidative stress. *Free radical research* **1999,** *31* (4), 273-300.
118. Singhal, R. K.; Anderson, M. E.; Meister, A., Glutathione, a first line of defense against cadmium toxicity. *The FASEB Journal* **1987,** *1* (3), 220-223.
119. Pompella, A.; Visvikis, A.; Paolicchi, A.; De Tata, V.; Casini, A. F., The changing faces of glutathione, a cellular protagonist. *Biochemical pharmacology* **2003,** *66* (8), 1499-1503.
120. Estrela, J. M.; Ortega, A.; Obrador, E., Glutathione in cancer biology and therapy. *Critical reviews in clinical laboratory sciences* **2006,** *43* (2), 143-181.
121. Forman, H. J.; Zhang, H.; Rinna, A., Glutathione: overview of its protective roles, measurement, and biosynthesis. *Molecular aspects of medicine* **2009,** *30* (1-2), 1-12.
122. Purkait, K.; Ruturaj; Mukherjee, A.; Gupta, A., ATP7B binds ruthenium (II) p-Cymene half-sandwich complexes: Role of steric hindrance and Ru–I coordination in rescuing the sequestration. *Inorganic chemistry* **2019,** *58* (22), 15659-15670.
123. Sarkar, A.; Acharya, S.; Khushvant, K.; Purkait, K.; Mukherjee, A., Cytotoxic Ru II-p-cymene complexes of an anthraimidazoledione: halide dependent solution stability, reactivity and resistance to hypoxia deactivation. *Dalton Transactions* **2019,** *48* (21), 7187-7197.
124. Povse, V. G.; Olabe, J. A., Kinetics and mechanism of ligand interchange in the [RuIII (edta) L] complexes; L= Cysteine and related thiolates. *Transition Metal Chemistry* **1998,** *23* (6), 657-662.

125. van Rixel, V. H.; Busemann, A.; Göttle, A. J.; Bonnet, S., Preparation, stability, and photoreactivity of thiolato ruthenium polypyridyl complexes: Can cysteine derivatives protect ruthenium-based anticancer complexes? *Journal of Inorganic Biochemistry* **2015,** *150*, 174-181.
126. Vargiu, A. V.; Robertazzi, A.; Magistrato, A.; Ruggerone, P.; Carloni, P., The hydrolysis mechanism of the anticancer ruthenium drugs NAMI-A and ICR investigated by DFT− PCM calculations. *The Journal of Physical Chemistry B* **2008,** *112* (14), 4401-4409.

127. Guo, W; Zhang, W; Luo, Q; LI, X; Zhao, Y; Xiong, S; Qang, F., Transferrin Serves As a Mediator to Deliver Organometallic Ruthenium(II) Anticancer Complexes into Cells. *Inorganic Chemistry* **2013**, *52(9)*, 5328-5338.